

# Contents

<b>1</b>	<b>Searches for New Physics in <math>\tau^+\tau^-</math> Final States</b>	<b>2</b>
1.1	Signal Modelling . . . . .	3
1.1.1	Additional Higgs Bosons . . . . .	3
1.1.2	Vector Leptoquarks . . . . .	6
1.2	Event Selection . . . . .	9
1.2.1	Trigger Requirements . . . . .	9
1.2.2	Offline Requirements . . . . .	10
1.3	Signal Extraction . . . . .	12
1.4	Background Modelling Overview . . . . .	16
1.5	QCD Estimation in the $e\mu$ Channel . . . . .	18
1.6	Embedding Method . . . . .	19
1.7	Fake Factor Method . . . . .	21
1.7.1	Determination Regions . . . . .	21
1.7.2	Parametrisation . . . . .	23
1.7.3	Corrections . . . . .	27
1.7.4	Applying Fake Factors . . . . .	28
1.8	MC Corrections . . . . .	31
1.9	Uncertainty Model . . . . .	32
1.9.1	Shape uncertainties . . . . .	32
1.9.2	Normalization uncertainties . . . . .	39
1.9.3	Uncertainties specific to $e\mu$ channel . . . . .	42
1.10	Postfit Plots . . . . .	44
1.11	Model Independent Results . . . . .	47
1.11.1	Limit Setting . . . . .	47
1.11.2	Significance and Compatibility . . . . .	47
1.11.3	2D Likelihood Scans . . . . .	47
1.12	Model Dependent Limits . . . . .	51

# Chapter 1

## Searches for New Physics in $\tau^+\tau^-$ Final States

The  $\tau^+\tau^-$  final states are a powerful tool to search for new physics at collider experiments. As the heaviest lepton, they are sensitive to resonant production of new neutral particles where the couplings have mass hierarchy. They are also sensitive to non-resonant effects from new physics mediators. This chapter will detail the searches for two such areas of new physics: additional Higgs bosons and vector leptoquarks. These searches are split up into three sections:

- i) A model independent search for single narrow spin-0 resonance,  $\phi$ , produced via gluon fusion ( $gg\phi$ ) or in association with a bottom quark ( $bb\phi$ ). The SM Higgs boson is treated as a background. The Yukawa couplings that contribute to the gluon fusion loop are set to SM values.
- ii) A search for the MSSM Higgs sector, in a number of benchmark scenarios. The benchmark scenarios are defined in Section 1.1.1. The production of SM Higgs boson is also used to constrain the available phase space.
- iii) A search for the t-channel exchange of a  $U_1$  vector leptoquark. Two scenarios are taken, based of the best fit to the b anomalies. These scenarios are detailed in Section 1.1.2.

These searches are performed with the full run-2 dataset ( $138\text{ fb}^{-1}$ ) collected by the CMS experiment. The search for additional Higgs bosons had previously been performed with data collected in 2016 ( $39\text{ fb}^{-1}$ ) and results were consistent with the SM background prediction.

## 1.1 Signal Modelling

### 1.1.1 Additional Higgs Bosons

Extended Higgs sectors, such as that of the MSSM, can be probed by direct searches for the additional bosons and further precise measurements of the Standard Model Higgs boson. This search for an extended Higgs sector is motivated by Type II 2HDMs, such as the MSSM. In these models  $\tan\beta$  enhances couplings of additional Higgs bosons to bottom-like quarks and leptons, whilst top-like couplings are suppressed. This narrows down the most important production modes of the Higgs boson into two categories: Gluon fusion and production in association with a bottom quark. Examples of these are shown in Figure 1.1.

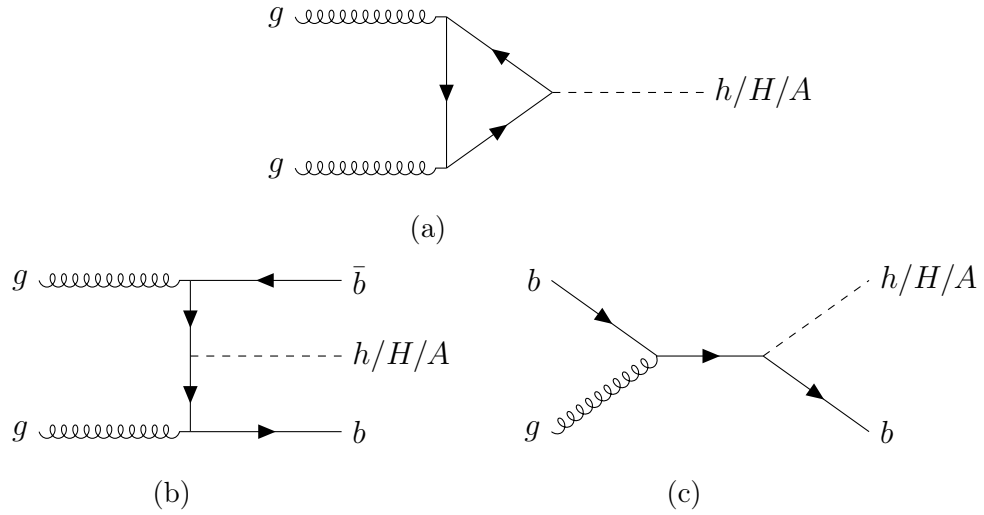


Figure 1.1: Diagram (a) shows the production of neutral Higgs bosons from gluon fusion. The dominant loop contributions to this diagrams are from top-only, bottom-only and top-bottom interference. Diagrams (b) and (c) show production in association with b quarks.

With the  $\tan\beta$  enhancement, the decays of additional Higgs bosons to tau leptons and bottom quarks are most likely. Tau leptons are identified with a higher purity than bottom quarks at the CMS detector. It is also easier to separate  $\tau^+\tau^-$  from the large QCD multijet background produced from the high energy proton-proton collisions. This hypothesis was tested with the 2016 dataset and although no deviations were observed, the strongest limits on the MSSM phase space was placed by the  $\tau^+\tau^-$  final states.

For this analysis, the production of additional Higgs bosons over a mass range of 60 GeV to 3.5 TeV are generated. Gluon fusion is simulated at NLO precision

using the 2HDM implementation of POWHEG 2.0. The kinematic properties are highly dependent on the contributions to the loop, which vary dependent on the specific signal model. To account for the different loop contributions at the NLO plus parton shower prediction, weights based off the  $p_T$  spectra are calculated to split the contributions from the t quark only, b quark only, and tb-interference. Once individual templates have been determined for each contribution to the loop, the 2HDM samples can be scaled to the correct specific MSSM scenario prediction by the following formula.

$$\begin{aligned} \frac{d\sigma_{\text{MSSM}}}{dp_T} = & \left( \frac{Y_{t,\text{MSSM}}}{Y_{t,2\text{HDM}}} \right)^2 \frac{d\sigma_{2\text{HDM}}^t(Q_t)}{dp_T} + \left( \frac{Y_{b,\text{MSSM}}}{Y_{b,2\text{HDM}}} \right)^2 \frac{d\sigma_{2\text{HDM}}^b(Q_b)}{dp_T} + \\ & \left( \frac{Y_{t,\text{MSSM}} Y_{b,\text{MSSM}}}{Y_{t,2\text{HDM}} Y_{b,2\text{HDM}}} \right) \left\{ \frac{d\sigma_{2\text{HDM}}^{t+b}(Q_{tb})}{dp_T} - \frac{d\sigma_{2\text{HDM}}^t(Q_{tb})}{dp_T} - \frac{d\sigma_{2\text{HDM}}^b(Q_{tb})}{dp_T} \right\} \quad (1.1) \end{aligned}$$

where  $Q_i$  are resummation scales that depend on the mass of the additional Higgs boson. Further contributions from any Supersymmetric partners have been checked and account for less than a few percent and so are neglected. This is also done separately for the scalar and pseudoscalar additional Higgs bosons, as the  $p_T$  distributions can differ. The MSSM benchmark scenarios considered are detailed in Ref. [1]. The scenarios provide the relative Yukawa couplings (to calculate the cross sections) and branching fractions of the MSSM Higgs bosons. An example of the changes to gluon fusion production, in the MSSM  $M_h^{125}$  scenario with  $m_A = 1600$  GeV and  $\tan\beta$  varying is shown in Figure 1.2. The distributions peak at a higher  $p_T$  for the top quark loop, therefore at smaller  $\tan\beta$ , where the top quark contribution is dominant, an additional Higgs boson would be more boosted.

Production in association with bottom quarks is simulated at NLO precision using the corresponding POWHEG 2.0 implementation in the four-flavour scheme. All additional Higgs boson signal generation is performed using the parton distribution function (PDF) NNPDF3.1. Tau lepton decay, parton showering and hadronisation are all modelled with the PYTHIA event generator where the PU profile is matched to data. All events generated are passed through a GEANT4-based simulation of the CMS detector and reconstructed in the same way as data.

The model dependent search for the MSSM also looks to find differences from the observed SM Higgs boson and the predicted MSSM SM-like Higgs boson. In each MSSM benchmark scenario, an uncertainty of  $\pm 3$  GeV is given on the prediction for the SM Higgs boson mass. This uncertainty is to reflect the contribution from any

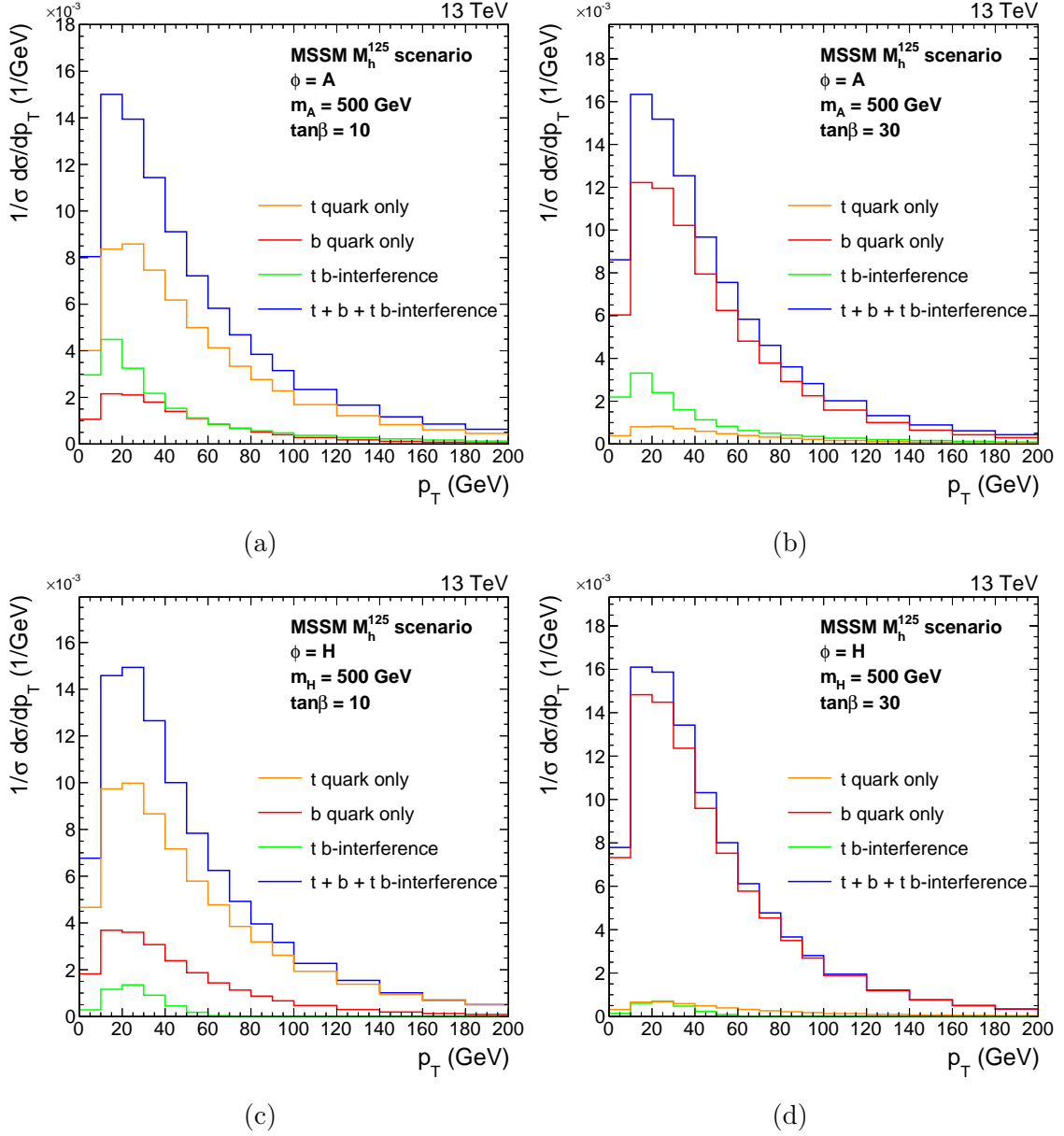


Figure 1.2:  $p_T$  density distributions of the  $A$  (top) and  $H$  (bottom) boson, with contributions to the gluon fusion loop displayed individually and summed. These are shown for  $\tan\beta$  values of 10 (left) and 30 (right) where  $m_A = 500$  GeV in the MSSM  $M_h^{125}$  scenario.

unknown higher-order corrections. The value of the mass is allowed to vary within this window, however the Yukawa couplings are rescaled the observed mass.

### 1.1.2 Vector Leptoquarks

The best fit in the vector leptoquark phase space to the B anomalies yielded large bottom quark and tau lepton couplings to the  $U_1$  particle. The possible production modes of a  $\tau^+\tau^-$  final state are shown in Figure 1.3.

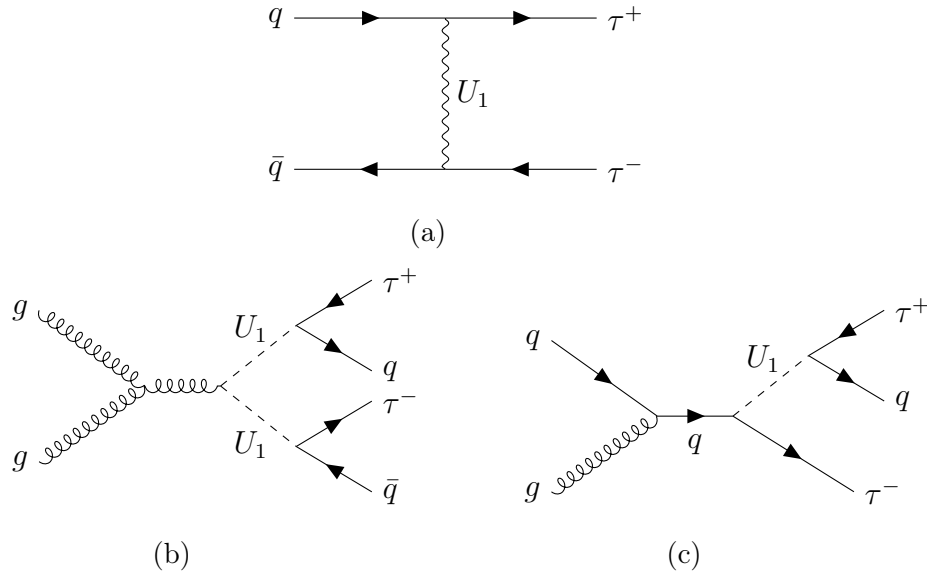


Figure 1.3: Feynman diagrams showing the contribution from  $U_1$  vector leptoquarks to the final state with a pair of oppositely charged tau leptons. Diagram (a) shows t-channel, (b) pair and (c) single production of a vector leptoquark.

Pair and single production of a vector leptoquark is dependent on its strong coupling, which is highly model dependent. For large mass,  $m_U$ , the probability of producing an on-shell  $U_1$  singlet or pair is heavily suppressed due to the momentum of the initial partons. These production processes are not discussed further in this search. Further studies have been used to search for single and pair production at the CMS experiment and no statistically significance derivation was observed.

The t-channel process contain two vertices with a  $U_1$  vector leptoquark, a quark and a tau lepton, and hence the cross section will scale with  $g_U^4$ . From the best fit to B anomalies this vertex will be dominated by the b quark and hence the initial state will be mostly from  $b\bar{b}$ , with sub-dominant contributions from  $b\bar{s}$ ,  $s\bar{b}$  and  $s\bar{s}$ . Although there are no additional b quarks in the final state in the LO process, initial state radiation can lead to additional b quarks in the final state. In this search the two scenarios discussed in Section ?? are considered. The only non negligible

parameter for  $\tau^+\tau^-$  final states from the fit in the  $m_U$ - $g_U$  phase space is the  $\beta_L^{s\tau}$  parameter. This is set to the best fit value.

The signal process of the  $U_1$  t-channel exchange is simulated in the five-flavour scheme (5FS) at LO precision using the MADGRAPH5\_aMC@NLO event generator, v2.6.5. Events are generated with one or fewer outgoing partons from the matrix element and the MLM prescription is then used for matching, with a scale set to 40 GeV. Negligible dependence of the  $U_1$  decay width ( $\Lambda$ ) is observed, for simulation this is chosen to approximately match the value predicted by the B anomaly fit. Samples with a mass between 1 and 5 TeV at  $g_U = 1$  are generated.

The interference between the  $U_1$  signal and  $Z/\gamma^* \rightarrow \tau\tau$  production was checked. A large destructive affect is observed, with the magnitude dependent on  $g_U$ . To account for this, separate samples are produced for this interference, generated in the same way as the t-channel exchange. The interference samples are then split into two with a di-tau mass split in order to have a sufficient number of events in the high di-tau mass regions. The cross section of these interference samples scale with  $g_U^2$ . Examples of the generator level di-tau mass distributions are shown in Figure 1.4.

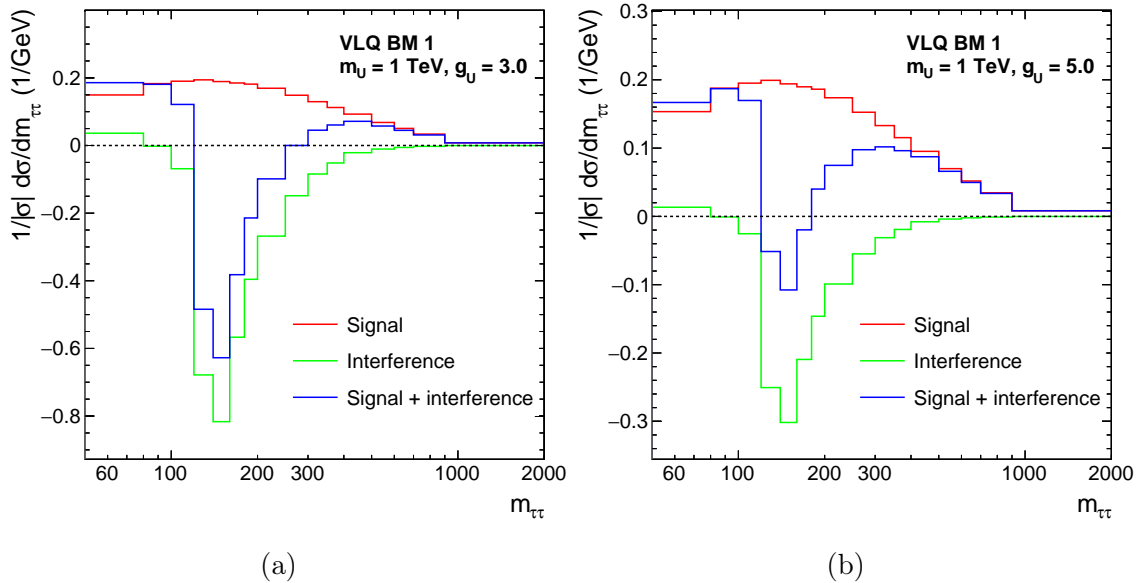


Figure 1.4: The generator level  $m_{\tau\tau}$  density distributions of the t-channel vector leptoquark signal and the interference with Drell-Yan. This is shown in the VLQ BM 1 scenario for a leptoquark of mass 1 TeV for coupling strengths of  $g_U = 3$  (a) and  $g_U = 5$  (b).

The t-channel signal produces a broad distribution in  $m_{\tau\tau}$  due to its non-resonant nature. The interference is mostly a destructive effect (except for at small  $m_{\tau\tau}$ ), with the yield becoming less negative at higher  $m_{\tau\tau}$ . The interference peaks negatively between 100 and 200 GeV and in this region the combined yield can be negative. Due to the difference in scaling of the two effects, at small  $g_U$  the interference is more dominant than the signal and hence the yield of the combined result is reduced.



## 1.2 Event Selection

The possible decays of two tau leptons and their branching fractions, where the tau decay is grouped into three categories  $e$ ,  $\mu$  and  $\tau_h$  as defined in Section ??, are shown in Table 1.1. For this search the four largest branching fraction channels used:  $\tau_h\tau_h$ ,  $e\tau_h$ ,  $\mu\tau_h$  and  $e\mu$ . This accounts for approximately 94% of di-tau events. The two same lepton channels are neglected due to small branching ratio and the dominating  $Z \rightarrow ee$  and  $Z \rightarrow \mu\mu$  backgrounds.

Channel	Branching Fraction
$\tau_h\tau_h$	42.0%
$e\tau_h$	23.1%
$\mu\tau_h$	22.6%
$e\mu$	6.2%
$ee$	3.2%
$\mu\mu$	3.0%

Table 1.1: Branching fractions of the decays of two tau leptons.

### 1.2.1 Trigger Requirements

In the four final state pairs a number of different online trigger requirements are needed. In the  $\tau_h\tau_h$  channel, two possible triggers are available: the double- $\tau_h$  and single- $\tau_h$  triggers. The single- $\tau_h$  trigger has a high  $p_T$  threshold at 120 (180) GeV for events recorded in 2016 (2017-2018), whilst the double- $\tau_h$  has a  $p_T$  threshold at 40 GeV. Therefore, the double- $\tau_h$  trigger is used individually where the  $\tau_h$  has  $p_T$  is below the single- $\tau_h$  threshold and the union of single- $\tau_h$  and double- $\tau_h$  triggered events are taken above the threshold.

In the  $e\tau_h$  and  $\mu\tau_h$  channels, there are three possible triggers available: the single- $e/\mu$ , single- $\tau_h$  and the  $e/\mu$ - $\tau_h$  cross-trigger. The cross-trigger is used for events where the light lepton has  $p_T$  between the thresholds for the cross-trigger and single- $e/\mu$  shown in Table 1.2. The light lepton used in the cross-trigger is required to be in the central barrel of the detector within  $|\eta| < 2.1$ . Above these light lepton  $p_T$  thresholds the single- $e/\mu$  trigger is used, where here it is required that the  $\tau_h$  has  $p_T > 30$  GeV. At  $\tau_h$   $p_T$  above the single- $\tau_h$  thresholds, the single- $\tau_h$  trigger is used in combination with the single- $e/\mu$  trigger.

Year/ Trigger	$e\tau_h$ cross-trigger	single- $e$	$\mu\tau_h$ cross-trigger	single- $\mu$
2016	23	26	20	23
2017	25	28	20	25
2018	25	33	21	25

Table 1.2: Lower trigger light lepton thresholds  $p_T$  in GeV for the  $e\tau_h$  and  $\mu\tau_h$  channels.

In the  $e\mu$  channel, there are three possible triggers available: the single- $e$ , single- $\mu$  and the  $e\mu$  cross-trigger. However, only the cross-trigger is used in this analysis, due to the larger efficiencies of correctly selecting light leptons. The  $e$  and  $\mu$  are required to have  $p_T > 15$  GeV and  $|\eta| < 2.4$ .

### 1.2.2 Offline Requirements

All offline selections stated are in addition the object selection discussed in Section ???. In this analysis, hadronic tau candidates are required to pass the **Medium**  $D_{\text{jet}}^{\text{WP}}$ .  $D_e^{\text{WP}}$  and  $D_\mu^{\text{WP}}$  are dependent on the channel. The **VVLoose**, **Tight**, **VVLoose**  $D_e^{\text{WP}}$  and the **VLoose**, **VLoose** and **Tight**  $D_\mu^{\text{WP}}$  are used in the  $\tau_h\tau_h$ ,  $e\tau_h$  and  $\mu\tau_h$  channels respectively. The tighter working point for the same light lepton discrimination as tagged in the event is used to remove light leptons faking hadronic taus from the  $Z \rightarrow ll$  process. The light lepton isolation requirement is  $I_{\text{rel}}^{e/\mu} < 0.15$  except for in the  $e\mu$  channel where the muon is required to have  $I_{\text{rel}}^\mu < 0.2$ .

The selected  $\tau$  lepton decay candidates are required to have opposite charge and to be separated by more than  $\Delta R > 0.5$  in all channels except  $e\mu$  where  $\Delta R > 0.3$ . In events where the numbers of an object in the event is greater than the required number of objects in the  $\tau\tau$  decay channel, the objects are sorted by the maximum  $D_{\text{jet}}^{\text{score}}$  if  $\tau_h$  or minimum  $I_{\text{rel}}$  if a light lepton and the leading objects are chosen. In order to maintain orthogonality between channels, events with additional light leptons passing looser selections than the nominal requirements, are rejected from the selection. The looser selections help to suppress the  $Z \rightarrow ll$  background process further.

In the  $e\tau_h$  and  $\mu\tau_h$  channels, a cut is placed at 70 GeV on the transverse mass between the light lepton  $\vec{p}_T$  and the missing  $\vec{p}_T$ , where the transverse momentum is

defined as,

$$m_T(\vec{p}_T^i, \vec{p}_T^j) = \sqrt{2p_T^i p_T^j (1 - \cos \Delta\phi)}, \quad (1.2)$$

where  $\Delta\phi$  is the azimuthal angle between  $\vec{p}_T^i$  and  $\vec{p}_T^j$ . The variable is used to remove  $W + \text{jets}$  background events, where a jet fakes a hadronic tau and the MET and light lepton from the  $W$  decay are aligned and hence the event has a large  $m_T(\vec{p}_T^{e/\mu}, \vec{p}_T^{\text{MET}})$ . In the  $e\mu$  channel an additional cut is placed on a variable named  $D_\zeta$ , which is defined as,

$$D_\zeta = p_\zeta^{\text{miss}} - 0.85p_\zeta^{\text{vis}}; \quad p_\zeta^{\text{miss}} = \vec{p}_T^{\text{miss}} \cdot \hat{\zeta}; \quad p_\zeta^{\text{vis}} = (\vec{p}_T^e + \vec{p}_T^\mu) \cdot \hat{\zeta} \quad (1.3)$$

where  $\vec{p}_T^{e/\mu}$  corresponds to the transverse momentum vector of the electron or muon and  $\hat{\zeta}$  to the bisectonal direction between the electron and the muon in the transverse plane [?]. A diagram of the inputs is shown Figure 1.5.

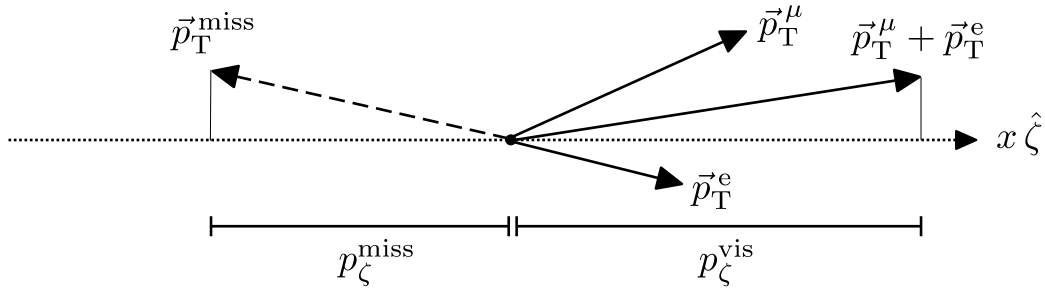


Figure 1.5: Diagram of inputs to the  $D_\zeta$  variable.

The linear combination is optimised for genuine di-tau events to peak around  $D_\zeta = 0$  GeV. It is motivated by the expectation that in di-tau decays from a resonance, the visible and missing (from tau neutrinos) momentums are roughly aligned and of similar magnitudes. In  $W + \text{jets}$  and  $t\bar{t}$  events the directions of the visible and missing products are expected to be more randomly distributed and lead to a non-peaking  $D_\zeta$ . Therefore only events with  $D_\zeta > -35$  GeV are considered for signal events. No b tagged events with this cut are vetoed and b tagged events with this cut are used for a  $t\bar{t}$  control region and discussed further in Section 1.4.

### 1.3 Signal Extraction

The optimisation of the signal extraction depends on which of the three scenarios, set out at beginning of this section, is searched for. The components of the optimisation are named the high mass, low mass and SM Higgs optimisation procedures. For the model independent search (i) the high or low mass optimisation procedures are used depending on whether the mass of the resonance is greater or less than 250 GeV. The search for the MSSM Higgs sector (ii) uses the high mass or the SM Higgs optimisation procedures depending on whether the reconstructed di-tau mass  $m_{\tau\tau}$  is greater or less than 250 GeV. Finally, the search for vector leptoquarks (iii) uses only the high mass optimisation procedure. The procedures are discussed in detail below.

The high mass optimisation procedure follows what was done in Ref. [1]. Firstly each category is split into categories with no b tagged and with one or more b tagged events. This firstly helps target the additional Higgs boson production modes gluon fusion and b associated production respectively. Secondly, the initial state radiation of a t-channel vector leptoquark signal dominated by initial states of b quarks, can lead to additional b jets in the final state. The reduced backgrounds in b tagged events allows for a more sensitive vector leptoquark search in this category.

The  $e\tau_h$  and  $\mu\tau_h$  channels are further subdivided into categories depending on the transverse mass between the light lepton and missing transverse momentum vectors as defined in Equation 1.2. The corresponding categories are defined as:

- **Tight- $m_T$** :  $m_T(\vec{p}_T^{e/\mu}, \vec{p}_T^{\text{miss}}) < 40$  GeV;
- **Loose- $m_T$** :  $40 \leq m_T(\vec{p}_T^{e/\mu}, \vec{p}_T^{\text{miss}}) < 70$  GeV.

The majority of the signal events fall within the **Tight- $m_T$**  sub-category. The **Loose- $m_T$**  category is used improve the signal acceptance for resonant masses of  $m_\phi > 700$  GeV.

In the  $e\mu$  channel, is also subdivided into three signal categories based of the cuts on the variable  $D_\zeta$  as defined in Equation 1.3. The three categories are defined as:

- **Low- $D_\zeta$** :  $-35 \leq D_\zeta < -10$  GeV;
- **Medium- $D_\zeta$** :  $-10 \leq D_\zeta [\text{GeV}] < 30$  GeV;
- **High- $D_\zeta$** :  $D_\zeta [\text{GeV}] \geq 30$  GeV.

By design, the majority of signal events are located in the **Medium- $D_\zeta$**  sub-category. The Low and High- $D_\zeta$  categories are used to catch the tail of the signal distributions. A schematic of all high mass optimisation categories are shown in Figure 1.6.

	No b tag			b tag		
$e\mu$	Low- $D_\zeta$	Medium- $D_\zeta$	High- $D_\zeta$	Low- $D_\zeta$	Medium- $D_\zeta$	High- $D_\zeta$
$e\tau_h$	Loose- $m_T$		Tight- $m_T$	Loose- $m_T$		Tight- $m_T$
$\mu\tau_h$	Loose- $m_T$		Tight- $m_T$	Loose- $m_T$		Tight- $m_T$
$\tau_h\tau_h$						
$t\bar{t}(e\mu)$				$D_\zeta < -35 \text{ GeV}$		
	Signal region (SR)					
	Control region					

Figure 1.6: Overview of the categories used for the extraction of the signal in the high mass optimisation procedure.

Once all category divisions have been applied, events are drawn in histograms based off a discriminating variable. The discriminating variable used in this analysis is  $m_T^{\text{tot}}$  and is defined below.

$$m_T^{\text{tot}} = \sqrt{m_T(\vec{p}_T^{\tau_1}, \vec{p}_T^{\text{miss}})^2 + m_T(\vec{p}_T^{\tau_2}, \vec{p}_T^{\text{miss}})^2 + m_T(\vec{p}_T^{\tau_1}, \vec{p}_T^{\tau_2})^2}, \quad (1.4)$$

where  $\tau_1$  and  $\tau_2$  refer to the visible products of the two tau leptons decays. This variable provides excellent discriminating power between higher mass resonant signals compared to other non-peaking backgrounds whilst still maintaining some separation between signal masses. It is also excellent at separating the high mass non-resonant di-tau signatures where a di-tau mass is unphysical for the signal, due to the use of the  $p_T$ s and in the variable. For the t-channel signal with the mediator has high mass, no significant mass separation is expected in any variable.

The low mass optimisation procedure loosely follows the high mass procedure with a few key difference. Firstly categories that are only sensitive to high mass signals are dropped. This includes the Low- $D_\zeta$  and Loose- $m_T$  categories. Each no b tag subcategory is further divided into four bins of reconstructed di-tau visible  $p_T$  with bin edges: 0,50,100,200 and  $\infty$ . This is not done in the b tag subcategories due to

the lack of statistics in this region. A schematic of the categories used in the low mass optimisation procedure is shown in Figure 1.7.

	No b tag		b tag	
$e\mu$	Medium- $D_\zeta$ $p_T^{\tau\tau} < 50$ GeV	High- $D_\zeta$ $p_T^{\tau\tau} < 50$ GeV	Medium- $D_\zeta$	High- $D_\zeta$
	$50 < p_T^{\tau\tau} < 100$ GeV	$50 < p_T^{\tau\tau} < 100$ GeV		
	$100 < p_T^{\tau\tau} < 200$ GeV	$100 < p_T^{\tau\tau} < 200$ GeV		
	$p_T^{\tau\tau} > 200$ GeV	$p_T^{\tau\tau} > 200$ GeV		
$e\tau_h$	Tight- $m_T$ $p_T^{\tau\tau} < 50$ GeV $50 < p_T^{\tau\tau} < 100$ GeV $100 < p_T^{\tau\tau} < 200$ GeV $p_T^{\tau\tau} > 200$ GeV		Tight- $m_T$	
$\mu\tau_h$	Tight- $m_T$ $p_T^{\tau\tau} < 50$ GeV $50 < p_T^{\tau\tau} < 100$ GeV $100 < p_T^{\tau\tau} < 200$ GeV $p_T^{\tau\tau} > 200$ GeV		Tight- $m_T$	
$\tau_h\tau_h$	Tight- $m_T$ $p_T^{\tau\tau} < 50$ GeV $50 < p_T^{\tau\tau} < 100$ GeV $100 < p_T^{\tau\tau} < 200$ GeV $p_T^{\tau\tau} > 200$ GeV			
$t\bar{t}(e\mu)$			Control region $D_\zeta < -35$ GeV	

Signal region (SR)

Control region

Figure 1.7: Overview of the categories used for the extraction of the signal in the low mass optimisation procedure.

The final difference with the high mass optimisation procedure is the discriminator used, here the reconstructed di-tau mass is used. This helps to separate signal events from the Z boson peak in this region. Examples of the signal mass separations in the  $\tau_h\tau_h$  channel with the low and high mass discriminators are shown in Figure ??

FIGURES OF DISTRIBUTIONS VLQ AND INTERFERENCE GGH AND BBH heavy GGH AND BBH light

Finally the SM Higgs optimisation procedure is taken from the CMS SM  $H \rightarrow \tau\tau$

analysis. This was previously used for simplified template cross section measurements. This uses a neural-network-based (NN) to obtain the most precise estimates from data of the SM Higgs produced via gluon fusion, vector boson fusion or vector boson associated production. The NN based analysis introduces 26 categories, 8 of which are optimised to pull the out the Higgs boson signal. Although the NN is trained specifically to target events with an SM-like Higgs boson, signal events with differing masses can also enter the NN categories.

## 1.4 Background Modelling Overview

The analysis considers several backgrounds including Drell-Yan,  $t\bar{t}$ ,  $W$ +jets, QCD, di-boson, single-top, and electroweak  $W$  and  $Z$  bosons production. These are split into a five categories:

- i) Events containing only genuine tau leptons.
- ii) Events with a jet misidentified as a hadronic tau ( $\text{jet} \rightarrow \tau_h$ ) in the  $e\tau_h$ ,  $\mu\tau_h$  or  $\tau_h\tau_h$  channels.
- iii) Events with jets faking both light leptons ( $\text{jet} \rightarrow l$ ) in the  $e\mu$  channel.
- iv) Events from  $t\bar{t}$  with a prompt light lepton ( $e$  or  $\mu$  not from a  $\tau$  decay) and the other object (if there are not two prompt light lepton) is from a genuine tau leptons.
- v) Other events. This is a small contribution and hence why it is grouped.
  - Non  $t\bar{t}$  events with a prompt light lepton ( $e$  or  $\mu$  not from a  $\tau$  decay) and the other object (if there are not two prompt light lepton) is from a genuine tau leptons.
  - Events with a light lepton faking a hadronic tau and the other object (if there are not two light leptons faking a hadronic tau) are reconstructed as prompt light lepton or from genuine tau leptons.
  - Events with a jet faking a light lepton and the other object is from genuine tau leptons in the  $e\tau_h$ ,  $\mu\tau_h$  or  $\tau_h\tau_h$  channels.
  - Events with one jet faking a light lepton and the other object from a prompt light lepton in the  $e\mu$  channel.

Backgrounds from (i) consists of largely  $Z/\gamma^* \rightarrow \tau\tau$  events but there are also smaller contributions from other processes. This background is modelled by a data-simulation hybrid method called the embedding method and this is described in detail in Section 1.6. Group (ii) is dominated by QCD,  $W$  + jets and  $t\bar{t}$  events with a  $\text{jet} \rightarrow \tau_h$  misidentification. This is modelled from data by the fake factor method ( $F_F$ ) and is explained in Section 1.7. Group (iii) is modelled from data to describe QCD multijet contribution to the background in the  $e\mu$  channel. The method to obtain this background is described in Section 1.5. The data driven background estimations for (i), (ii) and (iii) contribute  $>98\%$  of all expected background events in the  $\tau_h\tau_h$  channel,  $>90\%$  in  $e\tau_h$  and  $\mu\tau_h$  channels and  $>50\%$  in the  $e\mu$  channel.



The final groups, (iv) and (v), are modelled with MC. The  $t\bar{t}$  process is separated due to its large contribution to the phase space where a b jet is required.

The  $W + \text{jets}$  and  $Z \rightarrow ll$  processes are simulated at leading order (LO) using the MADGRAPH5\_aMC@NLO 2.2.2 (2.4.2) event generator [?, ?] for the simulation of the data taken in 2016 (2017–2018). To increase the number of simulated events in regions of high signal purity, supplementary samples are generated with up to four outgoing partons in the hard interaction. For diboson production, MADGRAPH5\_aMC@NLO is used at next-to-LO (NLO) precision. In each case, the FxFx [?] (MLM [?]) prescription is used to match the NLO (LO) matrix element calculation with the parton shower model. For  $t\bar{t}$  [?] and (t-channel) single top quark production [?], samples are generated at NLO precision using POWHEG 2.0 [?, ?, ?, ?]. The POWHEG version 1.0 at NLO precision is used for single top quark production in association with a W boson (tw channel) [?].

When compared with data,  $W + \text{jets}$ ,  $Z \rightarrow ll$ ,  $t\bar{t}$ , and single top quark events in the tW channel are normalised to their cross sections at next-to-NLO (NNLO) precision [?, ?, ?]. Single top quark (t-channel) and diboson events are normalized to their cross sections at NLO precision or higher [?, ?, ?].

## 1.5 QCD Estimation in the $e\mu$ Channel

The QCD model in the  $e\mu$  channel, that attempts to model events where two jets are misidentified as an electron muon pair, is taken from data with same sign electron muon pair with a transfer factor ( $F_T$ ). The transfer factor determines differences from the same sign to opposite sign region is calculated from a sideband region with an anti-isolated muon ( $0.2 < I_{\text{rel}}^\mu < 0.5$ ).  $F_T$  is initially parameterised by the  $\Delta R$  between the electron and muon, and the number of jets in the event, however additional dependencies on the electron and muon  $p_T$  enter via a correction.

Good agreement is observed in events with no b jets, for the discriminating variables discussed in Section 1.3, when applying  $F_T$  onto same sign events compared to opposite sign events where both regions have an anti-isolated muon. However in events with b jets, an additional correction is needed. This is determined to be 0.75 (differs very slightly between data taking years). As this correction is large, it is validated by switching the light lepton anti-isolation, so that the electron is required to have  $0.15 < I_{\text{rel}}^e < 0.5$ . Also events where both light leptons are anti-isolated are looked at. The correction for b tagged events is equivalent in all three regions, and a global average of the three is taken for the final correction.

To understand the physical reason for the large difference in no b tag and b tag events in same sign and opposite pairs, studies were performed on simulated samples. It was observed that the electron muon pair is usually produced from pairs of heavy quarks,  $pp \rightarrow b\bar{b}$  ( $c\bar{c}$ ). If the two jets are initiated from the heavy quarks there is a large bias towards opposite sign jets due to the opposite signs of the quark anti-quark pair. However if one of the heavy quarks is tagged as a b jet, another object has to be the jet initiator (a radiated gluon for example) and there is therefore no charge preference in the pair. As  $F_T$  is originally fit inclusively in numbers of b jets and the 0 bin is dominant, the correction over predicts the opposite sign to same sign ratio and so a large correction is needed as observed.

## 1.6 Embedding Method

The background for genuine di- $\tau$  lepton pairs is modelled via the embedding method. This is a hybrid method that utilises both data and MC techniques to produce high statistic samples, where the bulk of the event comes from data. This minimises both the chance of MC fluctuations and the size of the uncertainties. The background is dominated by  $Z \rightarrow \tau\tau$  decay however there will be smaller contributions from  $t\bar{t}$  and di-boson processes.

The algorithm first selects  $\mu\mu$  events from data. The selection is chosen to naturally target the pure  $Z \rightarrow \mu\mu$  region but still be loose enough to catch events from other processes, so not to introduce a bias on the  $Z$  boson mass. Events are required to pass the DoubleMuon trigger with minimum requirements on the invariant mass of the two muons ( $m_{\mu\mu}$ ) and the  $p_T$  of the leading and trailing muon. Also required at the trigger level is a loose association of the track to the PV and a loose isolation in the tracker. Offline objects matched to the trigger muons, are then required to have standard  $d_z$  and  $\eta$  selections and originate from a global muon-track, as defined in Section ???. The muon pair are required to have opposite charge and have  $m_{\mu\mu} > 20$  GeV. The fraction of processes within this selection is tested with MC background samples and a QCD model from same sign muon pairs with an extrapolation factor. Approximately 97% of selected events are expected to come from  $Z \rightarrow \mu\mu$  events with smaller contributions from  $Z \rightarrow \tau\tau$  ( $\tau \rightarrow \mu$ ), di-boson,  $t\bar{t}$  and QCD. The di-boson and  $t\bar{t}$  relative contributions are greater at higher  $m_{\mu\mu}$  and in events with tagged b jets whilst the QCD contribution is largest at lower  $m_{\mu\mu}$ . The events selected are biased by detector acceptances. Therefore, corrections on the reconstruction and identification efficiencies are performed in muon  $\eta$  and  $p_T$  using the "tag-and-probe".

Next, all energy deposits in the detector from the selected muons are removed. This involves removing the hits on global-muon track in the tracker, hits in the muons systems and clusters in the calorimeters that intercept the muon trajectory. Once completed, the selected muons and its kinematic properties are replaced with a tau lepton. To account for the difference in mass between the muon and tau, the muons are boosted into the center-of-mass frame of the di-muon system and then this 4-vector is taken for the tau but boosted back into the laboratory frame. The event simulation is performed from the PV. The tau lepton decay is then simulated with PYTHIA and separate samples are produced for differ  $\tau\tau$  decay channels. Only the decay of the tau leptons are then processed through the detector simulation and the

remainder of the  $\mu\mu$  event is added back. A schematic of the process is shown in Figure 1.8.

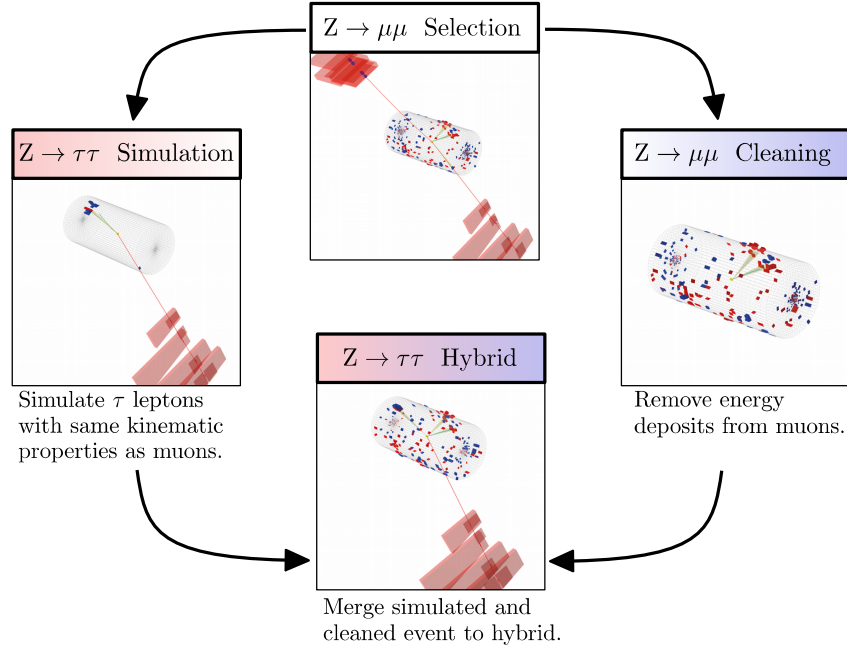


Figure 1.8: Schematic of the embedding method to model genuine di-tau backgrounds from di-muon events in data.

The embedding method is validated on dedicated samples, where the muons from data are replaced by simulated muons instead of taus.

## 1.7 Fake Factor Method

Backgrounds in which a jet fakes a  $\tau_h$  can be difficult to model using MC due to the poor description of the  $\text{jet} \rightarrow \tau_h$  fake rate in simulation. In addition, the small probability of a jet being misidentified as a  $\tau_h$  necessitates the production of high statistics MC samples at a significant computational expense. These shortcomings motivate the use of data-driven estimates for these processes. One such procedure is the fake factor ( $F_F$ ) method.

The  $F_F$  method utilises regions in the data to model the  $\text{jet} \rightarrow \tau_h$  background. Firstly, the determination regions, which are  $\text{jet} \rightarrow \tau_h$  enriched control regions orthogonal to the signal region. It is used to calculate  $F_F$  by taking the ratio of number of jet fake events that pass the nominal hadronic tau ID requirement ( $N(\text{Nominal})$ ), to the number of jet fake events that fail the nominal hadronic tau ID but pass a looser alternative hadronic tau ID requirement ( $N(\text{Alternative} \ \&\& \ !\text{Nominal})$ ), as shown in Equation 1.5.

$$F_F = \frac{N(\text{Nominal})}{N(\text{Alternative} \ \&\& \ !\text{Nominal})}. \quad (1.5)$$

In the remaining text this numerator and denominator are referred to as the pass and fail regions. The derivation of this ratio is done differentially with respect to key parameters that differ in the two regions. Once  $F_F$  have been derived it is common to calculate corrections in other sideband regions (a region orthogonal to the signal region) and combine  $F_F$  measured from different processes. Finally, the  $F_F$  are applied to the application region (AR). This is defined as the SR but with the criteria that the jet fakes fail the nominal hadronic tau ID but pass the looser alternative tau ID requirement. This now models the background from  $\text{jet} \rightarrow \tau_h$  events in SR.

The following Sections 1.7.1–1.7.4 detail the complexities of how this method is applied to this analysis. For these searches the nominal hadronic tau ID used is the **Medium**  $D_{\text{jet}^{\text{WP}}}$  and the alternative hadronic tau ID used is the **VVLoose**  $D_{\text{jet}^{\text{WP}}}$ .

### 1.7.1 Determination Regions

The fake factors are measured separately in each year of data taking period (2016, 2017, 2018), in each channel containing hadronic taus ( $e\tau_h$ ,  $\mu\tau_h$ ,  $\tau_h\tau_h$ ) and in enriched regions of dominant processes that contribute  $\text{jet} \rightarrow \tau_h$  events. In the  $e\tau_h$  and  $\mu\tau_h$  channels  $F_F$  are measured for three processes: QCD, W + Jets and  $t\bar{t}$ . In the  $\tau_h\tau_h$  channel  $F_F$  are measured only for the dominant QCD process. The QCD

process is assumed to produce two jet fakes and so the fake factors is chosen to be calculated from leading  $p_T$  hadronic tau candidate only. Section 1.7.4 discusses how single jet fake events in the  $\tau_h\tau_h$  channel are modelled.

Each separate measurement region is split into three sideband regions based off two cuts that surround the signal region. These regions are named the **Determination Region (C)**, **Alternative Determination Region (D)** and **Correction Region (B)** and are schematically shown in Figure 1.9.

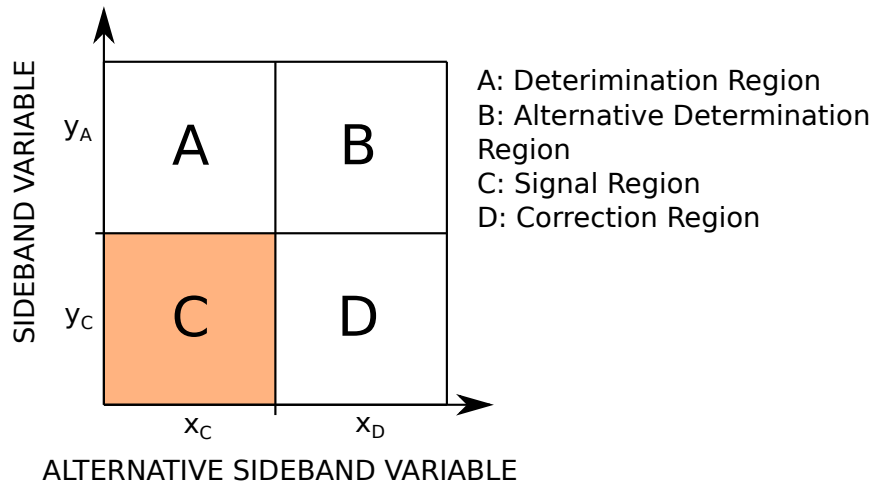


Figure 1.9: Schematic of the regions used for fake factor derivation.

Region A is used to measure and fit fake factors. Region B is an alternative region used to measure and fit fake factor to account for the difference in fake factors between A and C. These alternative fake factors are applied to the fail region in D and corrections are calculated comparing it to the pass region in D. The total fake factor per measurement region is calculated as the fake factors derived in region A multiplied by the correction calculated from region B to D.

The selection for  $x_C$ ,  $x_D$ ,  $y_C$  and  $y_A$ , as defined in Figure 1.9, in each separate measurement region are shown below. These are chosen to balance the number of events and the purity of each background in the region.

i)  $\tau_h\tau_h$  QCD

$y_C$ : The  $\tau_h$  candidates are required to have the opposite sign.

$y_A$ : The  $\tau_h$  candidates are required to have the same sign.

$x_C$ : The subleading tau passes the **Medium**  $D_{\text{jet}}^{\text{WP}}$ .

$x_D$ : The subleading tau fails the **VVLoose**  $D_{\text{jet}}^{\text{WP}}$  but passes the **VVLoose**  $D_{\text{jet}}^{\text{WP}}$ .

ii)  $e\tau_h$  and  $\mu\tau_h$  QCD

$y_C$ : The  $e/\mu$  and  $\tau_h$  candidates are required to have the opposite sign.

$y_A$ : The  $e/\mu$  and  $\tau_h$  candidates are required to have the same sign and the  $e/\mu$  to have  $I_{\text{rel}} > 0.05$ .

$x_C$ : The  $e/\mu$  candidate is required to have  $I_{\text{rel}} < 0.15$ .

$x_D$ : The  $e/\mu$  candidate is required to have  $0.25 < I_{\text{rel}} < 0.5$ .

iii)  $e\tau_h$  and  $\mu\tau_h$  W + Jets

$y_C$ : The  $m_T$  between the  $e/\mu$  and the MET  $< 70$  GeV.

$y_A$ : The  $m_T$  between the  $e/\mu$  and the MET  $> 70$  GeV and no b jets in the event.

$x_C$ : Data.

$x_D$ : W + Jets MC.

iv)  $e\tau_h$  and  $\mu\tau_h$   $t\bar{t}$ 

$y_C$ : Data.

$y_A$ : MC ( $t\bar{t}$  in B and W + Jets D).

$x_C$ :  $m_T < 70$  GeV.

$x_D$ :  $m_T > 70$  GeV and no b jets.

In the  $\mu\tau_h$  and  $e\tau_h$  channels QCD and W + Jets jet fake events are in general the most significant and contribute with approximately equal weights.  $t\bar{t}$  inclusively is small but becomes more significant when searching for events with a b jet. The additional  $I_{\text{rel}} > 0.05$  requirement in these channels for QCD is to reduce processes producing genuine leptons and the  $N_{\text{b-jets}} = 0$  requirement for W + Jets is to reduce  $t\bar{t}$  contamination. It is not possible to define a DR that is sufficiently pure in  $t\bar{t}$  events to make a reasonable measurement of  $F_F^{t\bar{t}}$  from data. Therefore  $F_F^{t\bar{t}}$  are derived from MC. A comparison of the  $F_F^{W+\text{jets}}$  measured in data and MC shows only  $\sim 10\text{--}20\%$  differences in the fake rates in data and MC. This observation coupled with the fact that the  $t\bar{t}$  contribution is small compared to the other processes means that any bias introduced by using  $F_F^{t\bar{t}}$  measured in MC is small compared to the uncertainties on the fake factors, discussed in Section ??.

## 1.7.2 Parametrisation

The raw  $F_F^i$  take into account dependencies on  $N_{\text{jets}}$  via the analysis tailed variable  $N_{\text{pre b-jets}}$ , the  $p_T$  of the  $\tau_h$  candidate ( $p_T^{\tau_h}$ ) and the  $p_T$  of the jet matched in  $\Delta R$  to

the  $\tau_h$  ( $p_T^{\text{jet}}$ ).  $N_{\text{pre b-jets}}$  is defined to map the dependence of  $F_F^i$  on  $N_{\text{jets}}$  and describe the categorising variable  $N_{\text{b-jets}}$  well. Although not local to the tau, it helps control other dependencies on the constituents of the event. It is the number of jets in the event with  $|\eta| < 2.4$  and  $p_T > 20$ . These are the same  $\eta$  and  $p_T$  thresholds required for a b-jet. The data is split into two bins of  $N_{\text{pre b-jets}}$ , equal to 0 and greater than 0. It is then further split by the ratio of  $p_T^{\text{jet}}$  to  $p_T^{\tau_h}$ . An example of the dependence of these two transverse momenta on the fake factor is shown in Figure 1.10.

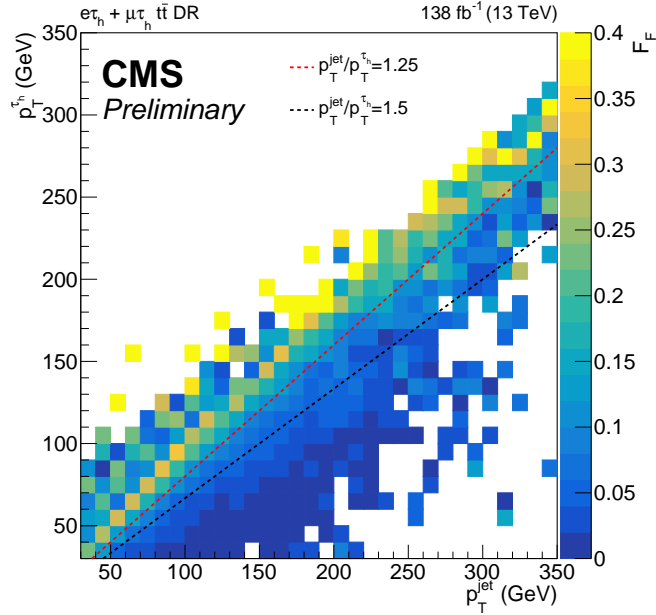


Figure 1.10: A 2D heat map of the fake factors determined from  $t\bar{t}$  MC for the full run-2 dataset in the combined  $e\tau_h$  and  $\mu\tau_h$  channels. This is shown with respect to the hadronic tau  $p_T$  and the  $p_T$  of the jet matched to the hadronic tau. The ratio of jet to hadronic tau  $p_T$  categorisation used is shown split by the dashed lines.

It is motivated by the observation that the fake factor is largest when the  $p_T^{\text{jet}}$  and  $p_T^{\tau_h}$  are closest. The physical motivation for this is when they are close, the hadronic tau candidate is likely to be isolated from any other hadronic activity and so more likely to be identified as a tau. However, when  $p_T^{\text{jet}}$  is larger than  $p_T^{\tau_h}$ , the candidate is likely surrounded by other hadronic activity and so more likely to be a jet fake. When  $p_T^{\text{jet}}$  is less than  $p_T^{\tau_h}$ , charge pions are likely not close enough to the PV to be clustered into the jet and so the event is more likely to be classified as a jet fake. This will then lead to the fake factor dependence as seen in Figure 1.10.

For all divisions of the phase space, dependence on the  $p_T^{\tau_h}$  is fit using the superposition of a Landau and a zeroth order polynomial in the low- $p_T$  region. The fake factors are seen to rise sharply at high- $p_T$ . This increase happens in either the bin



$140 < p_T^{\tau_h} < 200$  GeV or  $p_T^{\tau_h} > 200$  GeV. To map this effect, binned values are taken based off the algorithm shown in Figure 1.11 and the fit is used below the minimum bin.

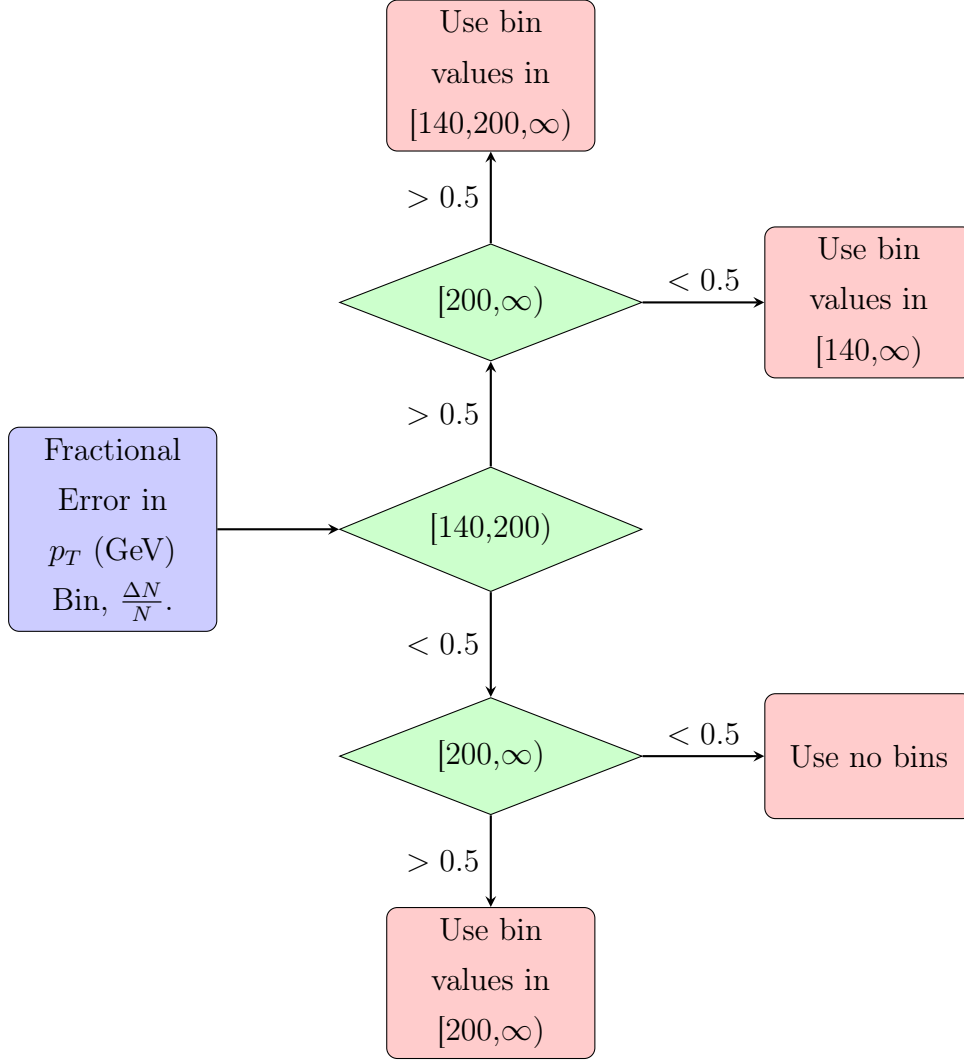


Figure 1.11: Flow chart of the algorithm used to determine where binned values are taken instead of the fit. The blue box represents the input, the green diamonds represent the decisions and the red boxes represent the outputs.

The Landau and zeroth order polynomial fits are flattened at  $p_T^{\tau_h}$  values where there is no significant downwards shift or at the final bin. Fake factor fits with respect to  $p_T^{\tau_h}$  are shown in Figures 1.12-1.13. The fake factors are highest in the lowest  $p_T^{\text{jet}}/p_T^{\tau_h}$  bin and lowest in the highest bin as expected. Otherwise the fake factors fall with  $p_T$  in each category until the thresholds used for the high  $p_T$  binning algorithm.

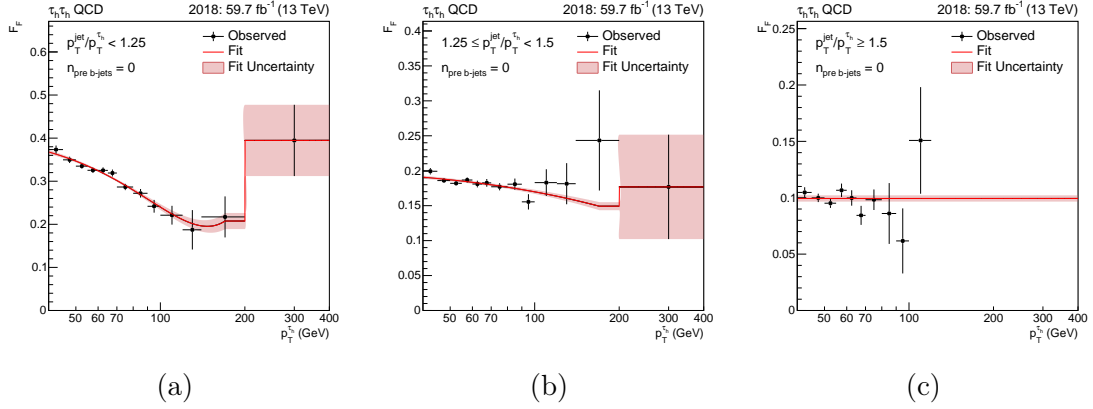


Figure 1.12: Fake factor fits in  $\tau_h\tau_h$  channel for the QCD  $N_{\text{pre b jets}} = 0$  category with 2018 data. The three jet  $p_T$  to hadronic tau  $p_T$  categories are shown.

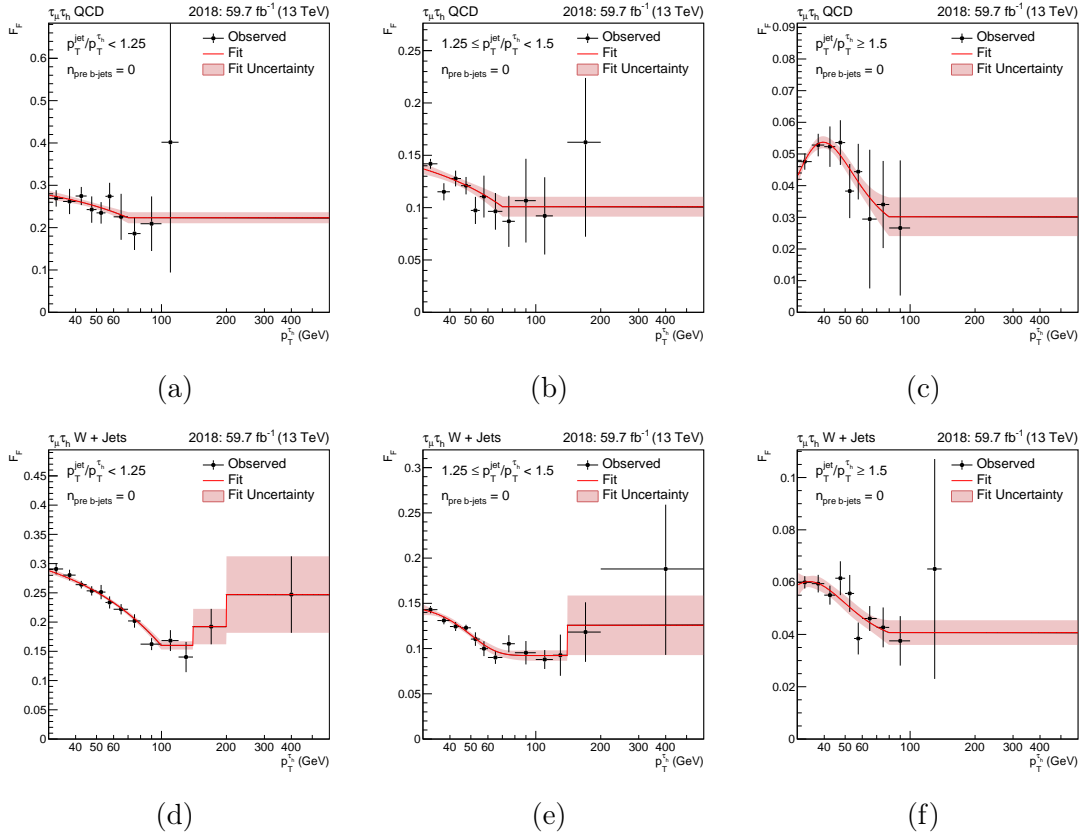


Figure 1.13: Fake factor fits in  $\mu\tau_h$  channel for the QCD and  $W + \text{Jets}$   $N_{\text{pre b jets}} = 0$  category with 2018 data. The three jet  $p_T$  to hadronic tau  $p_T$  categories are shown for each process.

### 1.7.3 Corrections

In the  $\tau_h\tau_h$  channel, the measured  $F_F^{\text{QCD}}$  are then corrected to account for non-closures in other variable in the **Determination Region**. The only significance non-closures are observed for  $E_T^{\text{miss}}$  related variables and are largest for events with  $N_{\text{pre b-jets}} = 0$ . Closure corrections are performed for the variable  $\Delta R$  in bins of  $N_{\text{b-jets}}$ . In the  $\mu\tau_h$  and  $e\tau_h$  channels, the measured  $F_F^{\text{QCD}}$  and  $F_F^{\text{W+jets}}$  are corrected for non-closures observed in the  $E_T^{\text{miss}}$  variables and  $p_T^{e/\mu}$  distributions. A study was performed to determine the nature of these non-closures and it was found that the cause was due to fake  $E_T^{\text{miss}}$  arising from mismeasurement of the energies of particles in a jet. A diagram of this effect is shown in Figure 1.14.

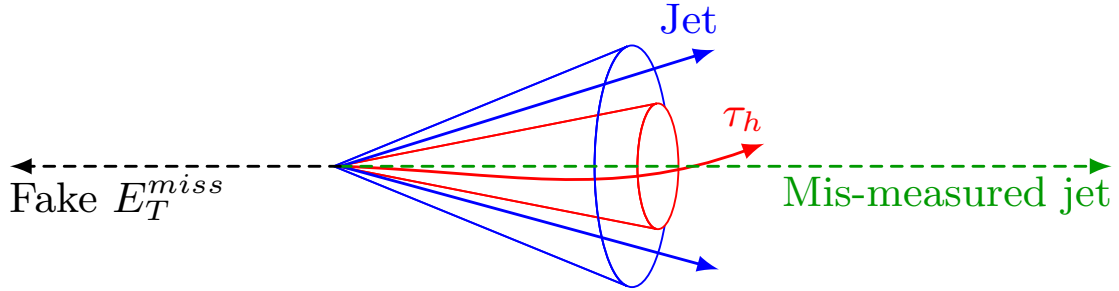


Figure 1.14: Diagram showing how fake  $E_T^{\text{miss}}$  arises from mismodelling jet constituents in hadronic tau identification.

To correct for this effect, the QCD fake factors are corrected as a function of  $C_{\text{QCD}}$ , where  $C_{\text{QCD}}$  is defined as,

$$C_{\text{QCD}} = \frac{E_T^{\text{miss}} \cos \Delta\phi(\vec{p}_T^{\text{miss}}, \vec{p}_T^{\tau_h})}{p_T^{\tau_h}}. \quad (1.6)$$

where  $\Delta\phi(\vec{p}_T^{\text{miss}}, \vec{p}_T^{\tau_h})$  is the separation in the azimuthal angle between the the missing  $\vec{p}_T^{\text{miss}}$  and  $\vec{p}_T^{\tau_h}$ . The numerator quantifies the missing transverse momentum in the direction of the hadronic tau candidate. Once divided by the  $\tau_h$   $p_T$ ,  $C_{\text{QCD}}$  is a measure of the fraction of missing to visible hadronic tau transverse momentum aligned with the hadronic tau. For  $W + \text{jets}$  and  $t\bar{t}$  the situation is slightly different due to the presence of genuine missing energy from neutrinos. In this case, the correction variable is modified to approximately subtract the genuine  $E_T^{\text{miss}}$  from the total. This approximation assumes the neutrino is back-to-back and balanced with the light lepton (which is exactly true for  $W$  bosons produce at rest in the transverse

direction). The equation then becomes,

$$C_W = \frac{(E_T^{\text{miss}} + p_T^{e/\mu}) \cos \Delta\phi(\vec{p}_T^{\text{miss}} + \vec{p}_T^{e/\mu}, \vec{p}_T^{\tau_h})}{p_T^{\tau_h}}. \quad (1.7)$$

When either correction variable is separated from 0, a larger quantity of fake  $E_T^{\text{miss}}$  is expected in the event. In these regions a large correction is needed due to the mis-measured jet energy spectrum shifting the hadronic tau candidate isolation and so shifting the tau identification scores. Examples of these closure corrections are shown in Figure 1.15

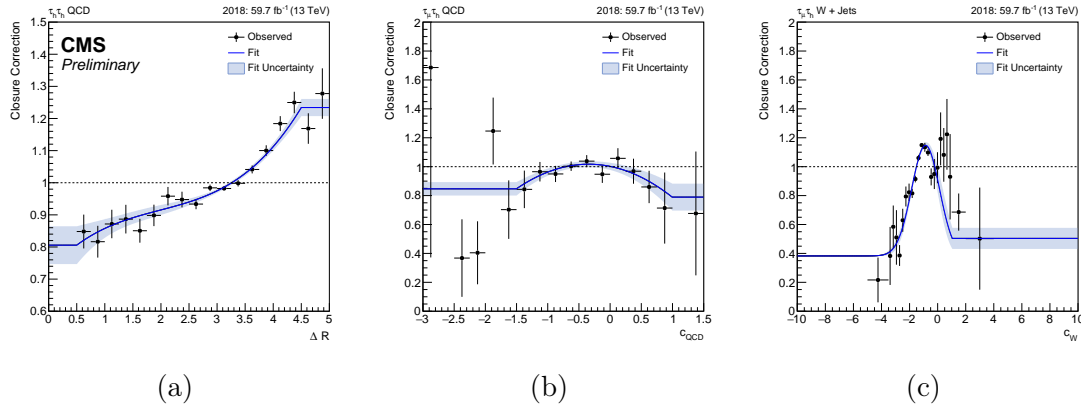


Figure 1.15: Determination region closure correction fits with 2018 data. (a) is the correction parametrised by  $\Delta R$  in events with  $N_{\text{b jets}} = 0$  in the  $\tau_h\tau_h$  channel. (b) and (c) show the correction for the  $\mu\tau_h$  channel parametrised by the specific correction variables defined in Equation 1.6 and 1.7 for QCD and W + jets processes respectively.

After the **Determination Region** is modelled well for all variables of interest, extrapolation corrections from the fake factors derived in B applied to region D are calculated. In the  $\tau_h\tau_h$  the correction is parameterised by the  $p_T$  of the leading hadronic tau candidate, in the  $e\tau_h$  and  $\mu\tau_h$  channels it is parameterised by the  $p_T$  of the light lepton. Where statistics allow, these corrections are calculated in the high mass optimisation procedure categories. Examples of the extrapolation corrections are shown in Figure 1.16.

#### 1.7.4 Applying Fake Factors

In the  $e\tau_h$  and  $\mu\tau_h$  channels the  $F_F^i$  measured for the different processes are combined into an overall factor,  $F_F$ , using

$$F_F = \sum_i f_i \cdot F_F^i, \quad (1.8)$$

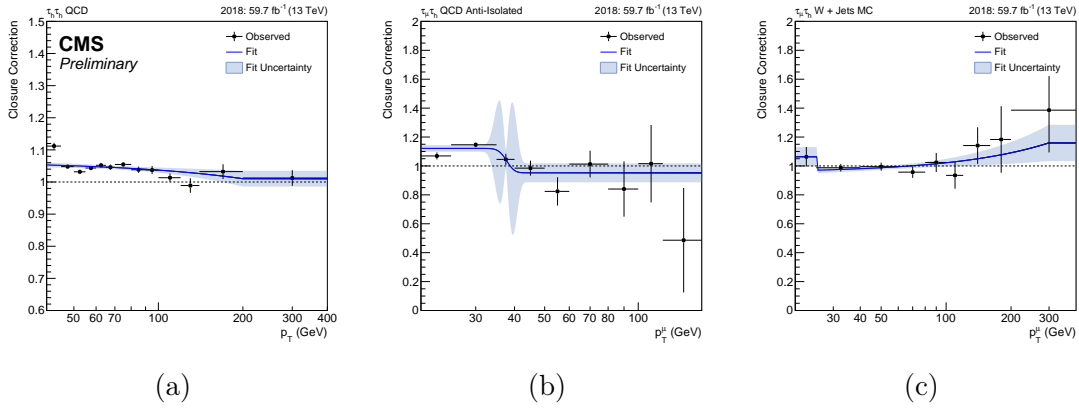


Figure 1.16: Determination region to application region closure correction fits with 2018 data. (a) is the correction moving from same sign to opposite sign tau leptons the parameterised by leading  $\tau_h p_T$  in events with  $N_{b\text{-jets}} = 0$  in the  $\tau_h \tau_h$  channel. (b) and (c) show the correction for the  $\mu \tau_h$  channel moving from same sign to opposite sign tau leptons and high  $m_T$  to low  $m_T$  both parameterised by the the muon  $p_T$  for QCD and W + jets processes respectively.

where the factor  $f_i$  is defined as

$$f_i = \frac{N_{\text{AR}}^i}{\sum_j N_{\text{AR}}^j}, \quad (1.9)$$

which is the fraction of events with a jet  $\rightarrow \tau_h$  originating from process  $i$  over the total number of jet  $\rightarrow \tau_h$  events for all processes in the application region. These fraction of events are estimated with MC, with a QCD model which is extrapolated from same sign tau pairs. It is observed that W + jets is the dominating process in this region, however there are effect from QCD at low  $m_T$  and from  $t\bar{t}$  in the b tagged categories. These fractions are then multiplied to the relevant corrected fake factor and applied to the fail region in C, with any events which are not jets faking hadronic taus subtracted off with MC.

For the  $\tau_h \tau_h$  channel there are two hadronic taus that a jet can fake. For this analysis, the fake factors are only applied the leading hadronic tau candidate failing the tau ID in C. This models all events where the leading hadronic tau candidate is a jet fake. However, this leaves a small fraction of events, where the leading candidate is a genuine tau and the sub-leading candidate is a jet fake. This contribution (mostly from W + jets) is added back with MC.

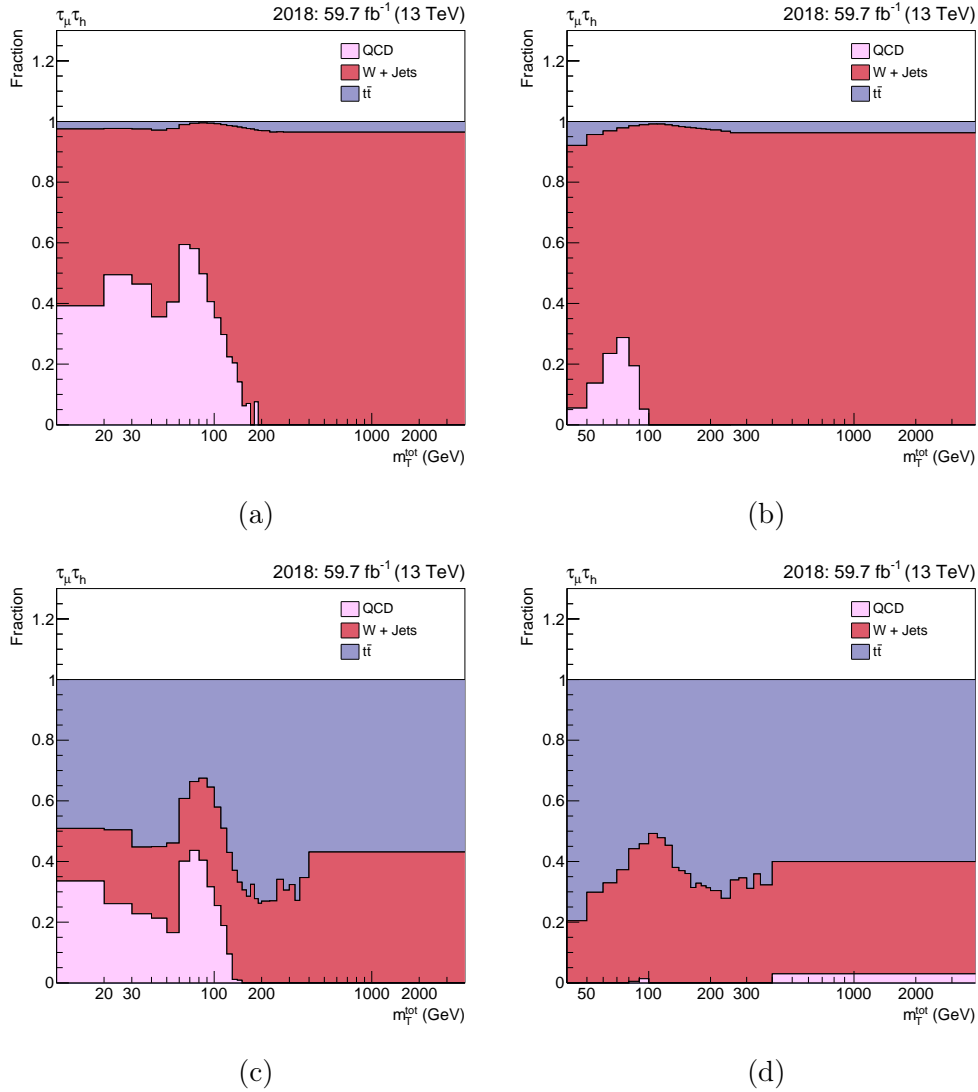


Figure 1.17: The expected application region fractions of the processes in the  $\mu\tau_h$  channel. (a) and (b) show the no b tag Tight- $m_T$  and Loose- $m_T$  categories and (c) and (d) show the b tag Tight- $m_T$  and Loose- $m_T$  categories respectively.

## 1.8 MC Corrections

## 1.9 Uncertainty Model

### 1.9.1 Shape uncertainties

The following uncertainties change the shape of the discriminator and so are shifted on an event-by-event basis.

- **Tau ID efficiency**

Binned uncertainties are applied as a function of  $p_T$  in the  $e\tau_h$  and  $\mu\tau_h$  channels, and of the tau decay mode in the  $\tau_h\tau_h$  channels. These vary between 3-9%. The uncertainty is uncorrelated between variable bins, correlated between decay channels and uncorrelated between years of data taking. To account for the different anti-lepton discriminator working points, an uncertainty of 3% per tau is applied and treated as uncorrelated between the channels. For the embedded samples the same uncertainty scheme on the tau ID SF is taken and 50% are correlated to MC uncertainties and 50% uncorrelated, because of the shared real data in the measurement.

- **Tau Trigger efficiency**

For hadronic taus, uncertainties in the trigger efficiencies differential in the transverse momentum of the hadronic tau leptons are used. The uncertainties are obtained from the fitted scale factors used to derive the corrections for the tau trigger efficiencies. For the tau legs of the double-tau and lepton+tau cross triggers separate nuisance parameters are implemented for the different reconstructed hadronic decay modes of the tau lepton, 1 prong decays (DM0), 1 prong decays with additional neutral pions (DM1 and DM2), 3 prong decays (DM10) and three prong decays with additional neutral pions (DM11).

For the single-tau trigger leg due to limited statistics it is not possible to determine scale factors and uncertainties split by decay mode and therefore a single uncertainty common to all decay modes is applied.

For the double-tau trigger we further split the hadronic trigger efficiencies in the  $p_T$  regions  $< 100$  GeV and  $> 100$  GeV to allow the fit more freedom to adjust the high  $p_T$  regions relative to the low  $p_T$  regions. The  $> 100$  GeV region represents the region where the trigger is maximally efficient and the scale factor is approximately constant, the fitted scale factors and uncertainties in this region are dominated by the high  $p_T$  bins used for the scale factor measurements so it is appropriate that it is decoupled from the  $p_T$  regions  $< 100$  GeV region where the scale factors and uncertainties are dominated by the low  $p_T$  bins.



The uncertainties are applied to all processes determined from simulated samples or the embedded samples. They are treated as 50 % correlated between the embedded and the simulated samples and uncorrelated across the channels. The uncertainties are treated as uncorrelated across the years, since different reconstruction algorithms and isolation criteria have been implemented at the HLT level, and the uncertainties are mainly statistical in nature.

- **Lepton trigger efficiency**

The uncertainty on the trigger efficiencies amounts to 2% per lepton in the  $e\tau_h$ ,  $\mu\tau_h$  and  $e\mu$  channels. They are basically normalization uncertainties but implemented as shape uncertainties as they only touch the events triggered by the corresponding cross trigger or single lepton triggers. These uncertainties are uncorrelated between channels as different triggers are used for each channel. The uncertainty is applied to all processes where the yield is estimated from MC and to the embedded samples. The embedded and MC uncertainties are uncorrelated. Due to the different trigger selections, the uncertainties on the lepton triggers are treated as uncorrelated between the eras.

- **Tau energy scale**

Shape uncertainties are applied that depend on the decay mode of the hadronic taus. The uncertainties range between 0.2 and 1.1 %. In the embedded samples we have hybrid events where the simulated taus might be mixed with calorimeter deposits remaining from the muon cleaning. For this reason, the tau energy scale for embedded samples is treated as 50% correlated with MC. This is done with separate nuisance parameters per decay mode. The uncertainties on the tau energy scale are treated as uncorrelated between 2016, 2017, 2018 data according to the current TauPOG recommendation.

- **Electron energy scale**

One uncertainty on the electron energy scale and resolution respectively is applied to MC using object specific information provided by the EGamma POG. For embedded samples this information is not reliable due to the energy regression run on low level MC quantities which have different conditions in embedded samples. Therefore, an energy scale uncertainty of 0.5 % for electrons in the barrel region and 1.25 % for electrons in the endcaps is applied following the previous EGamma recommendations. It is treated as uncorrelated to the uncertainties on MC because they are based on different estimation methods and due to the different conditions in the electron modeling. These uncertainties are treated as fully correlated between the eras according to the

EGamma recommendation [?].

- **Jet energy scale**

In general, the JetMET POG derives uncertainties on the jet energy scale from 27 (28) sources in 2016 (2017, 2018) and combines them in a single uncertainty with one nuisance parameter.

For this analysis, the sources are grouped according to a reduced scheme drafted by the JetMET group and which is motivated by the affected detector regions and also depending on the correlation between the data taking eras. This results in 11 nuisances for a single era, called Absolute, Absolute\_year, HF, HF\_year, BBEC1, BBEC\_year, EC2, EC\_year, RelativeBal, RelativeSample\_year, FlavorQCD. All nuisances with the suffix '\_year' are treated as uncorrelated between the years, the remaining ones as correlated. For all samples without recoil corrections applied, namely  $t\bar{t}$ , di-Boson and single top, the JES shifts are also propagated to the MET (i.e. PuppMET) and further to MET-dependent variables like  $m_{SV}$ , the fitted invariant mass of the di-tau system.

- **Jet energy resolution**

An uncertainty on the jet energy resolution retrieved from the provided module [?] is applied to MC samples and as for JEC propagated to the MET for all samples without recoil corrections applied. According to the JetMET recommendation, this uncertainty is treated as uncorrelated between years.

- **$l$  to  $\tau_h$  fake energy scale**

Uncertainty shifts are applied to the  $p_T$  of lepton to  $\tau_h$  fakes in MC samples uncorrelated between decay modes. The magnitude is 1.0% for muons in all eras. For electrons, more specific values for the uncertainties that depend on the era and detector region are provided by the Tau POG which range between 0.5 and 6.6 %. These uncertainties are uncorrelated between years.

- **MET unclustered energy uncertainty**

The MET unclustered energy uncertainty is applied to all MC processes that do not have recoil correction applied, namely the  $t\bar{t}$  and VV processes, as recommended by the JetMET POG. It is uncorrelated between the eras.

- **MET recoil correction uncertainties.**

For all MC processes that have recoil correction the hadronic response and its resolution are varied within the uncertainties determined during the compu-

tation of the recoil corrections. The recoil correction uncertainties are uncorrelated between the eras.

- **MET uncertainties in embedded events**

The uncertainties on the MET correction for embedded events are estimated by varying the clustered and unclustered energy uncertainties in the MC events used to derive the corrections. Statistical uncertainties on the measured correction factors are also taken into account.

- **Top  $p_T$  re-weighting**

Uncertainty between no and twice the correction on the re-weighting applied to  $t\bar{t}$  events in all channels. Fully correlated between all eras.

- **DY  $m_{\ell\ell}, p_T$  re-weighting**

To derive the uncertainty, a variation is introduced by not applying the correction weights and applying them twice. The one standard deviation uncertainty corresponds then to 10% of this variation and is applied to  $Z \rightarrow \ell\ell$  events in all channels. 2017 and 2018 are treated as correlated due to the same MC tune. 2016 is uncorrelated.

- **$t\bar{t}$  contamination in embedding**

Embedded samples replace part of the  $t\bar{t}$  background where two genuine taus are involved. An uncertainty on this  $t\bar{t}$  contamination in the embedded samples is applied. This shape uncertainty is created by adding/subtracting 10% of the genuine tau-pair fraction of the  $t\bar{t}$  MC sample to/from the embedded sample. This uncertainty is treated as correlated between the channels but uncorrelated between the eras due to the different double muon trigger menus for the selected data events.

- **$\tau_h$  tracking efficiency in embedding**

An uncertainty on the tracking efficiency of hadronic taus in the embedded samples is propagated fully correlated between the decay channels but uncorrelated between 1 and 3 prong decay modes. According to the TauPOG recommendation, it is treated as 50 % correlated between the eras.

- **Fake-factor uncertainties**

The backgrounds with jets misidentified as  $\tau_h$  are estimated from data with the fake factor method. There are different sources of uncertainty related to this method.

In the  $\tau_h\tau_h$  channel the following uncertainties are applied:

- Statistical uncertainties on the measured fake factors - these uncertainties are taken from the uncertainty bands on the fitted functions, split into two independent uncertainties using the procedure outlined in [?]. Due to the statistical nature of these uncertainties there are separate uncertainties for each  $N_{\text{jets}}/\text{jet } p_T$  bin and the uncertainties are treated as uncorrelated across years.
- Statistical uncertainties on the measured closure corrections - these uncertainties are taken from the uncertainty bands on the fitted functions, split into two independent uncertainties using the procedure outlined in [?]. Due to the statistical nature of these uncertainties there are separate uncertainties for each  $N_{\text{jets}}$  bin and the uncertainties are treated as uncorrelated across years.
- A systematic uncertainty due to the OS/SS extrapolation corrections - this uncertainty is defined by applying the correction twice for the upwards variation and not applying the correction for the downwards variations.
- Systematic uncertainties to account for differences between the fake factors measured for QCD events and non-QCD fake factors, since QCD fake factors are applied also for W+jets and  $t\bar{t}$  events in this channel. The uncertainties are 20 % for the W+jets contribution and 40 % for  $t\bar{t}$ .
- Systematic uncertainties on all non-closure corrections equal to the size of the corrections are applied (applying the closure correction twice for up, or not applying for down).
- With the closure tests there is some evidence of non-closures in the sub-leading  $\tau_h p_T$  and  $E_T^{\text{miss}}$  distributions, however additional closure correction are not applied since these don't seem to improve the description of the  $m_T^{\text{tot}}$  distributions. Therefore, the size of the non-closure in these variables is taken only as an uncertainty.
- A systematic uncertainty due to the choice of fit function to describe the fake factors. This is estimated by comparing to fake factors fitted with a first order polynomial set constant above 100 GeV.

In the  $\mu\tau_h$  and  $e\tau_h$  channels the following uncertainties are applied:

- Statistical uncertainties on the measured W+jet, QCD, and  $t\bar{t}$  fake factors - these uncertainties are taken from the uncertainty bands on the fitted

functions, split into two independent uncertainties using the procedure outlined in [?]. Due to the statistical nature of these uncertainties there are separate uncertainties for each  $N_{\text{jets}}/\text{jet } p_T$  bin and the uncertainties are treated as uncorrelated across years.

- Statistical uncertainties on the measured closure corrections - these uncertainties are taken from the uncertainty bands on the fitted functions, split into two independent uncertainties using the procedure outlined in [?]. Due to the statistical nature of these uncertainties there are separate uncertainties for each  $N_{\text{jets}}$  bin and the uncertainties are treated as uncorrelated across years.
- For the QCD fake factors a systematic uncertainty due to the OS/SS extrapolation corrections - this uncertainty is defined by applying the corrections twice for the upwards variation and not applying the correction for the downwards variations.
- For the QCD fake factors a systematic uncertainty due to the anti-iso  $\rightarrow$  iso extrapolation corrections. This uncertainty is defined by comparing the extrapolation from anti-iso  $\rightarrow$  iso using two methods. The first method (which is used for the nominal correction) bins the correction as a function of  $I_{\text{rel}}$  for the region with  $I_{\text{rel}} > 0.05$  which is dominated by QCD events, and then uses a linear extrapolation to determine the size of the correction in the  $I_{\text{rel}} < 0.05$  regions. The second method bins the correction as a function of  $I_{\text{rel}}$  using the full  $I_{\text{rel}}$  range, in this case there is a significant contribution from non-QCD events in the  $I_{\text{rel}} < 0.05$  region (mainly due to W+jets) which is accounted for by subtracting the non-QCD component using MC.
- For the W+jets fake factors a systematic uncertainty due to the high- $m_T \rightarrow$  low- $m_T$  extrapolation correction - this uncertainty is defined by applying the corrections twice for the upwards variation and not applying the correction for the downwards variations.
- For the  $t\bar{t}$  fake factors a systematic uncertainty to account for possible differences between the fake factors in MC and data (as the  $t\bar{t}$  fake factors are measured from MC) - this uncertainty is determined by comparing the fake factors derived for W+jets in data and MC. For the **b-tag** categories in the lowmass BSM analysis, an additional correction factor is derived as a function of  $m_{\tau\tau}$  to account for non-closures when applying the measured fake factors to simulated  $t\bar{t}$  events. We apply an additional

shape uncertainty in this case which is defined by applying the corrections twice for the upwards variation and not applying the correction for the downwards variations.

- Systematic uncertainties on all non-closure corrections equal to the size of the corrections are applied (applying the closure correction twice for up, or not applying for down).
- For the W+jets and QCD fake factors an uncertainty due to the subtraction of events from other processes when deriving the fake factors.
- A systematic uncertainty due to the choice of fit function to describe the fake factors. This is estimated by comparing to fake factors fitted with a first order polynomial set constant above 100 GeV.

- **Bin-by-bin uncertainties**

Statistical shape uncertainties in the backgrounds due to the use of Monte-Carlo and embedded samples or templates derived from data events with limited number of events are taken into account via the autoMCstats functionality of Combine.

- **Theory uncertainties**

For the  $gg\phi$  process, in particular for low mass hypotheses, the variation of `hdamp` parameter of the POWHEG MC generator as well as the  $\mu_R/\mu_F$  scale variations are used to determine the uncertainties on the  $p_T$  spectrum of each contribution at NLO QCD to the Higgs boson production via gluon fusion (top, bottom, top-bottom interference). These are also determined from additional samples produced up to the generator level, and applied as event weights dependent on generator level  $p_T$  after the parton shower simulation. These uncertainties are included as shape uncertainties as they may affect the shapes of the  $m_T^{\text{tot}}$  distribution as well as the predicted signal yields.

- **Embedding Z  $p_T$  and mass shape uncertainties**

For the embedded samples we observe some non-closures in the shapes of the  $p_T$  and mass distributions for a control samples of  $Z \rightarrow \mu\mu$  events, where muons in data are replaced by simulated muons. We therefore take these non-closures as an additional shape uncertainty as a function of the Z  $p_T$  and mass for our  $Z \rightarrow \tau\tau$  signal regions.

## 1.9.2 Normalization uncertainties

The following uncertainties are applied as log normal uncertainties on the yield of the affected processes.

- **Luminosity**

(1.2 %, 2.3 %, 2.5 %) luminosity uncertainty is applied to the (2016, 2017, 2018) [?][?][?] templates which originate from MC simulation. This uncertainty is partly correlated between eras according to the current recommendation by lumi experts. The different uncertainty sources and their magnitudes for each year are shown in Table 1.3.

Table 1.3: Luminosity uncertainties split by uncertainty source and data-taking period. Values taken from [?].

uncertainty source	2016	2017	2018
Uncorrelated	1.0 %	2.0 %	1.5 %
Correlated	0.6 %	0.9 %	2.0 %
Correlated (2017, 2018)	0.0 %	0.6 %	0.2 %

- **Electron, muon ID efficiency**

The estimated uncertainties on electron and muon scale-factors is 2%. This uncertainty is applied to all processes where the yield is estimated from MC. The same 2% uncertainty is also applied to the embedded events. 50% are correlated with the MC uncertainty and 50% uncorrelated because the measured data efficiencies entering the scale factors are same but efficiency measurements are separate for MC and embedded samples. These uncertainties are treated as fully correlated between the years.

- **Lepton to tau fake rate**

Uncertainties provided by the TauPOG that depend on the lepton  $\eta$  are applied. These are treated as being independent for each of the indicated detector sections. The effect on the shapes is negligible and therefore these uncertainties are converted to  $\ln N$ . The uncertainties are statistically dominated and therefore treated as uncorrelated between eras.

- **B-tagging efficiency**

The b-tagging scale-factors by the BTV POG are provided with uncertainties depending on the detector region. These are applied per jet to MC simulation using the promotion/demotion method. There are dedicated scale factors

for the b-tag efficiency and the fake rate which results in two corresponding nuisances. Shape effects are neglected by transforming the uncertainties into a pure normalization uncertainties, and these uncertainties are treated as uncorrelated between the years.

- **Prefiring**

Upper and lower bounds are taken from the efficiency maps provided by the L1 DPG and propagated on all MC samples as shape uncertainty for 2016 and 2017. The size of the uncertainty as the weight itself depends on the event topology. In general the uncertainty is at the order of 1%. It is correlated between eras and channels.

- **Background normalization uncertainty**

- A 2% uncertainty is applied to the  $Z \rightarrow ll$  process to account for the uncertainty on the Drell-Yan cross section fully correlated between the years.
- A 5% uncertainty is applied to the di-boson and single-top processes to account for the uncertainties on the production cross section fully correlated between the years.
- A 4% uncertainty is applied to the W+jets process to account for the uncertainty on the production cross section fully correlated between the years.
- A systematic uncertainty on the non-closure correction  $r_{\text{b-tag}}$  in b-tagged categories of the  $e\mu$  final state for the QCD estimate is taken into account as described in section ??, uncorrelated across data-taking years.
- Uncertainty on the MC acceptance extrapolation from the  $t\bar{t}$  control region to the  $t\bar{t}$  in the signal regions is determined. A 1% uncertainty is applied in the control region to account for variations in the variables used to select this control region. Extrapolation uncertainties due to different choices of factorisation and renormalisation scale are smaller than 1%, depending on the category.
- For the embedded samples an additional 4% uncertainty (2% per muon = 4%) fully correlated between the channels is applied to take account of efficiency of the double muon trigger that was used to select input events for the embedding technique. The uncertainties are decorrelated between



the years due to changes in the trigger setup used for selection of di-muon events between years.

- In cases where the SM Higgs boson is included as a background the following theoretical uncertainties on the cross sections and branching ratios are included:

The uncertainties on the ggH production cross-section recommended in YR4 are applied. The uncertainties on the cross-section include a 3.9% uncertainty due to variations of the QCD scales and a 3.2% uncertainty from PDF+ $\alpha_s$  variations.

The uncertainties on the VBF Higgs production cross-section recommended in YR4 are applied which include a 0.4% uncertainty from variations of QCD scales and a 2.1% uncertainty from PDF+ $\alpha_s$  variations. The uncertainties are fully correlated between years.

The uncertainties on the W(Z)H associated production cross-sections recommended in YR4 are applied which include a 1.9%(1.6%) uncertainty from the QCD scale variations and a 1.9%(1.6%) uncertainty from PDF+ $\alpha_s$  variations. The uncertainties are fully correlated between years.

The recommended uncertainties on the  $H \rightarrow \tau\tau$  branching fraction provided in YR4 are applied to all Higgs signal samples (ggH, VBF, and VH). These uncertainties include a 1.7% uncertainty due to missing higher order corrections, a 0.99% parametric uncertainty on the quark masses, and a 0.62% parametric uncertainty on  $\alpha_s$ .

The  $H \rightarrow WW$  contributions are also considered as background, and the corresponding branching ratio uncertainties provided are also taken into account.

## • Theory uncertainties

For the model-dependent  $m_A - \tan\beta$  limits theoretical uncertainties on the MSSM Higgs cross sections are included. This includes the pdf+ $\alpha_s$  and scale uncertainties that depend on the benchmark scenario considered,  $m_A$ , and  $\tan\beta$ , and are included in the model files [?].

For the  $b\bar{b}\phi$  signal process, theoretical uncertainties on the signal acceptance in terms of number of b-jets due to the parton shower matching are estimated by varying the `hdamp` parameter of the POWHEG MC generator used to create

the signal samples by factors of 2 and  $\frac{1}{2}$ . The additional samples are produced up to the generator level with parton showers with PYTHIA, such that generator level information on final state physics objects becomes available. The uncertainties are determined for 0 b-jet and  $\geq 1$  ( $= 1$ ) b-jet categories, for a few exemplary signal mass points, and interpolated to the full range of used signal masses. For the signal acceptance, the yields of varied samples are normalized to the same cross-section. The QCD scale uncertainty is used to probe the effect of higher-order terms not considered in the NLO calculations. This uncertainty is estimated by varying the renormalization ( $\mu_R$ ) and re-factorization ( $\mu_F$ ) scales by factors of 2 and  $\frac{1}{2}$  independently under the constrain  $\frac{1}{2} \leq \frac{\mu_R}{\mu_F} \leq 2$ . Since varying these scales will probe both the uncertainty on the cross-section as well as the signal acceptance the uncertainty on the cross-section must be factored out. This is done by normalizing each varied QCD scale to the fully-inclusive number of events for the default scale choice. The scale uncertainty is then taken as half the maximum difference in the signal acceptance. The uncertainties due to the QCD scale and `hdamp` variations are added linearly as recommended by the POWHEG authors. The resulting uncertainties on the **b-tag** category signal acceptance range between 1–6 % depending on the mass point. PDF uncertainties are also included. These uncertainties range between 1–2% for the **b-tag** category.

### 1.9.3 Uncertainties specific to $e\mu$ channel

Background estimates in the  $e\mu$  channel are affected by uncertainties in the jet  $\rightarrow e(\mu)$  and  $\mu \rightarrow e$  misidentification probabilities as discussed in Section ???. The uncertainty in the  $\mu \rightarrow e$  misidentification probability affects estimation of the Z+jets background with Z boson decaying into a pair of muons and has vanishing impact on estimation of other backgrounds. Uncertainties in the jet  $\rightarrow e$  and jet  $\rightarrow \mu$  misidentification probabilities affect mainly estimates of the W/Z+jets backgrounds with leptonically decaying W and Z bosons, and to a lesser extent estimates of the  $t\bar{t}$ , single-top and di-boson backgrounds. Typically, shape altering effect of these uncertainties is small and they are treated as log-normal uncertainties. Non-negligible shape altering effect is observed only for the jet  $\rightarrow e$  and  $\mu \rightarrow e$  misidentification probabilities in the background templates corresponding to the Z+jets production followed by  $Z \rightarrow ee(\mu\mu)$  decays. In these cases shape altering effects are taken into account.

For the QCD extrapolation method which is used to estimate the QCD multijet background in the  $e\mu$  final state ten uncertainties are applied. This includes uncer-

tainties on the extrapolation factor arising from the three parameters in the fit to the  $\Delta R(e\mu)$  dependence, binned in three jet bins. These uncertainties are uncorrelated between the eras. The tenth uncertainty describes uncertainties in the extrapolation of the correction factors from the anti-isolated to the isolated region and is treated as correlated between the years. These uncertainties have vanishing shape altering effect on the QCD background estimate and treated as log-normal ones.

The QCD background estimate is affected also by uncertainties in the  $\text{jet} \rightarrow e(\mu)$  misidentification probabilities and electron charge flip rate, as these uncertainties have an impact on the non-QCD background estimated from simulation and subtracted from data in the SS side band region to model QCD background shape as described in Section ???. For all these uncertainties shape altering effect on the QCD background estimate is negligible and uncertainties are treated as log-normal ones. Uncertainties in the  $\text{jet} \rightarrow e$  and  $\text{jet} \rightarrow \mu$  misidentification probabilities are fully correlated between signal categories of the  $e\mu$  channel and the SS sideband region, where shape of the QCD background is derived.

## 1.10 Postfit Plots

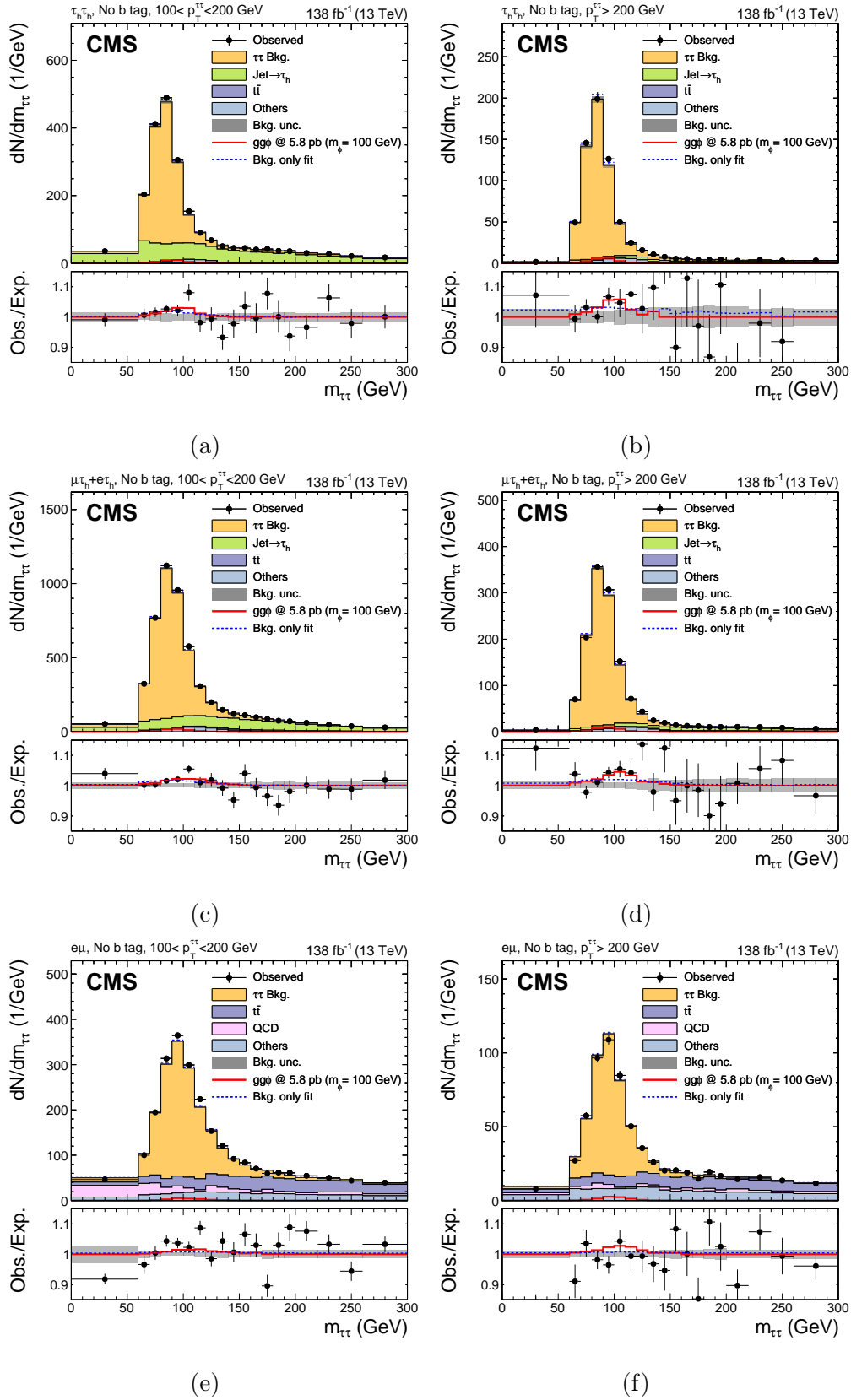


Figure 1.18: Distributions of  $m_{\tau\tau}$  in the no b tag second highest (left) and highest (right)  $p_T$  category for the  $\tau_h\tau_h$  (top), the combined  $e\tau_h$  and  $\mu\tau_h$  (middle) and the  $e\mu$  (bottom) channels. The solid histograms show the stacked background predictions after a signal plus background fit to the data. The best fit gluon fusion signal for  $m_\phi = 100$  GeV is shown by the red line. Also shown by a blue dashed line on the bottom pad is the ratio of the background predictions for the background only fit to the signal plus background fit

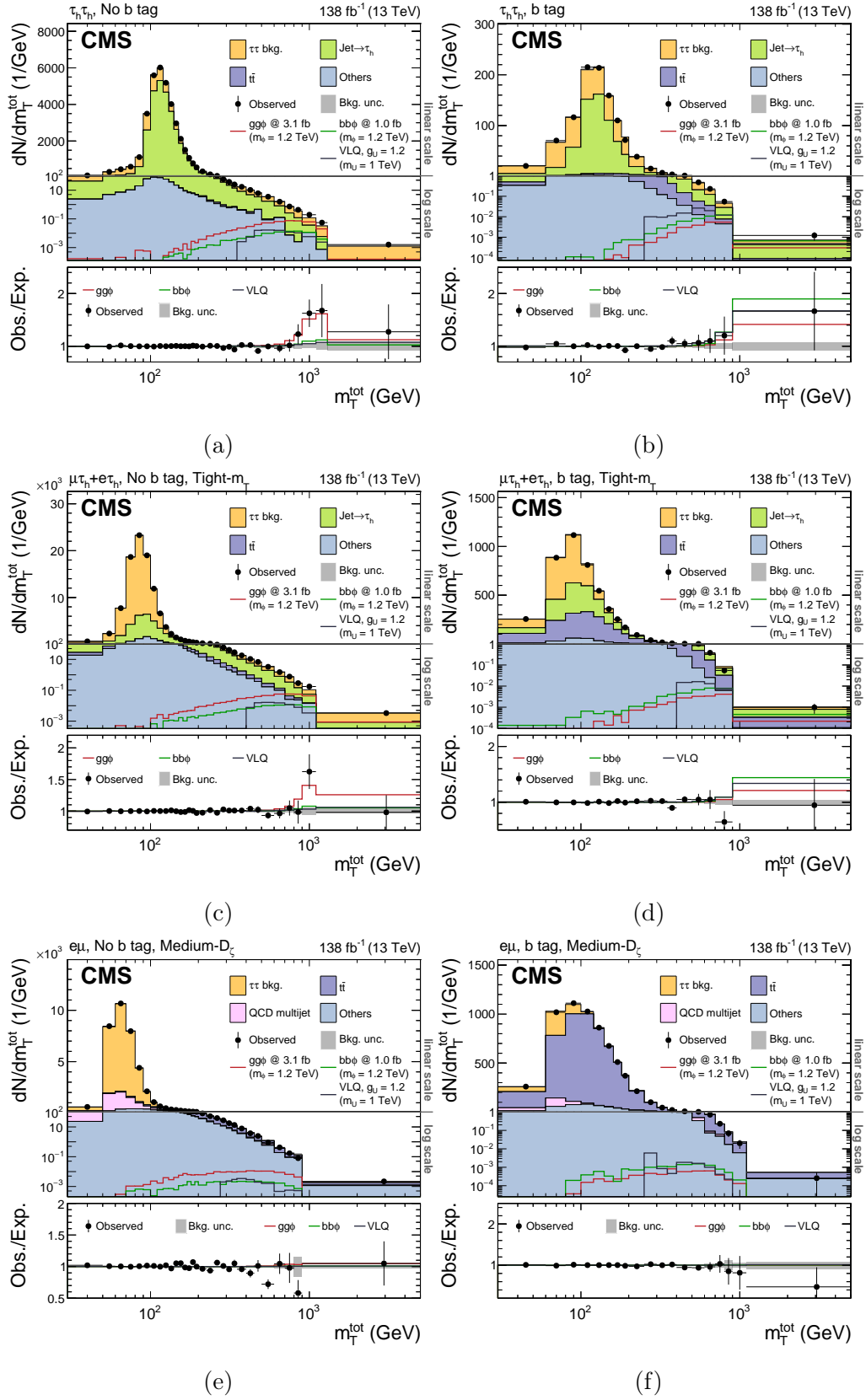


Figure 1.19: Distributions of  $m_T^{\text{tot}}$  in the  $\tau_h \tau_h$  no b tag (a) and b tag (b) categories, the combined  $e \tau_h$  and  $\mu \tau_h$  no b tag (c) and b tag (d) Tight- $m_T$  categories and the  $e \mu$  no b tag (e) and b tag (f) Medium- $D_\zeta$  categories. The solid histograms show the stacked background predictions after a background only fit to the data. The best fit gluon fusion signal for  $m_\phi = 1.2$  TeV is shown by the red line, b associated production and  $U_1$  signals are also shown for illustrative purposes.

## 1.11 Model Independent Results

### 1.11.1 Limit Setting

$$q_\mu = -2 \ln \left( \frac{\mathcal{L}(\text{data}|\mu, \hat{\theta}_\mu)}{\mathcal{L}(\text{data}|\hat{\mu}, \hat{\theta}_{\hat{\mu}})} \right), 0 \leq \hat{\mu} \leq \mu, \quad (1.10)$$

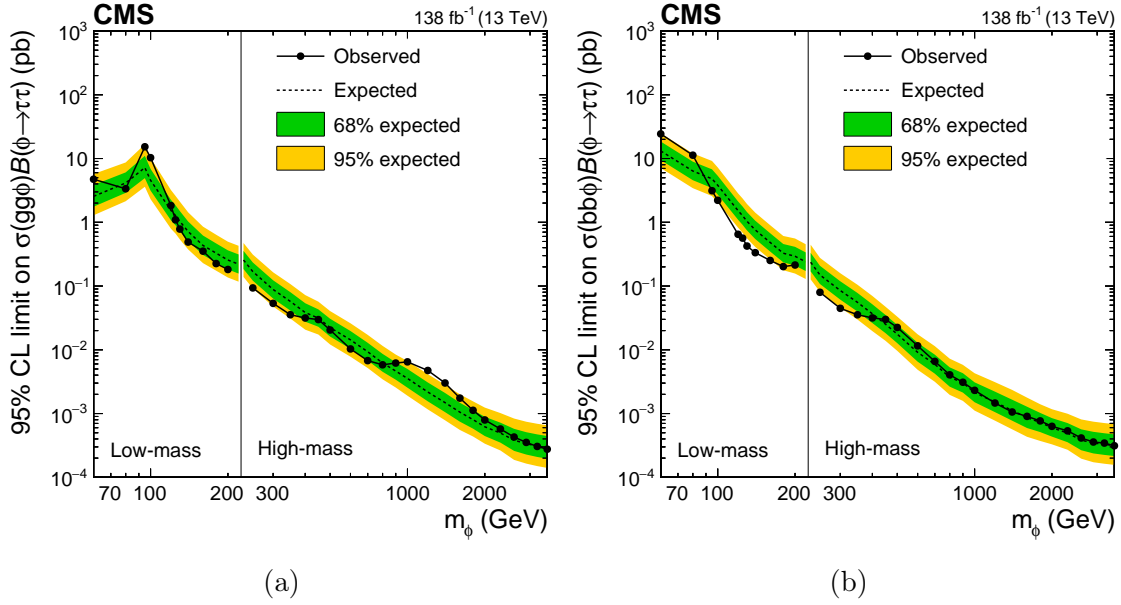


Figure 1.20: Model independent limits.

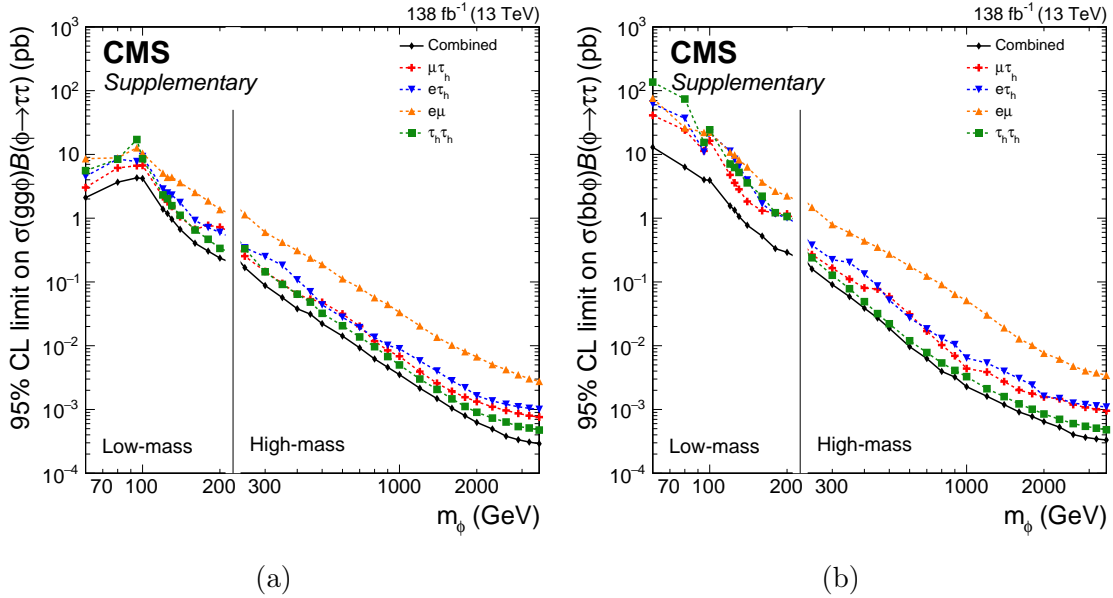


Figure 1.21: Model independent limits.

### 1.11.2 Significance and Compatibility

### 1.11.3 2D Likelihood Scans

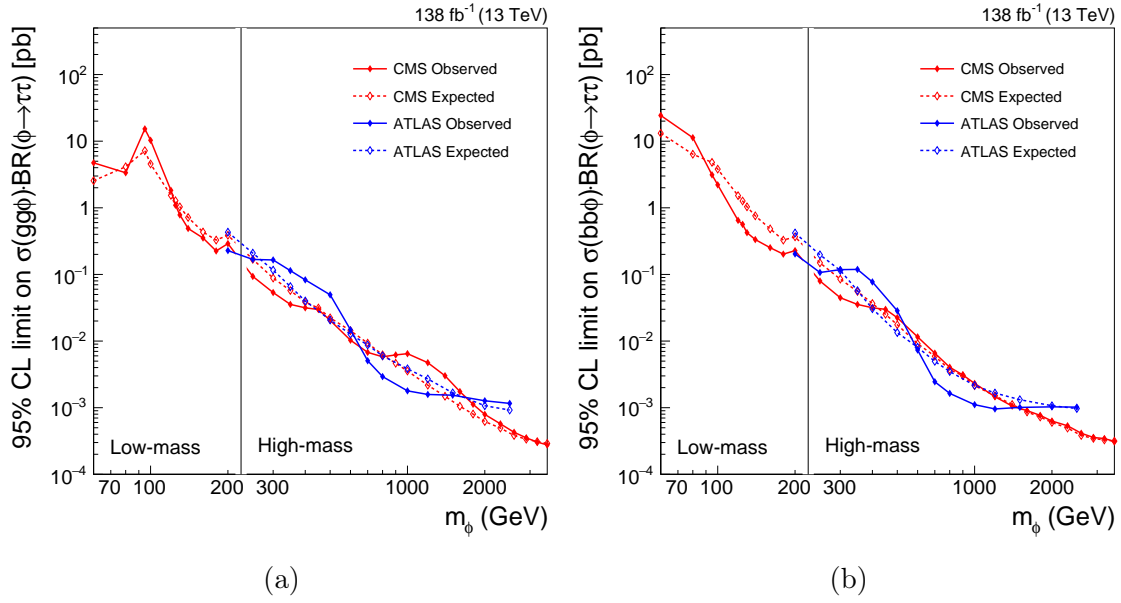


Figure 1.22: Model independent limits.

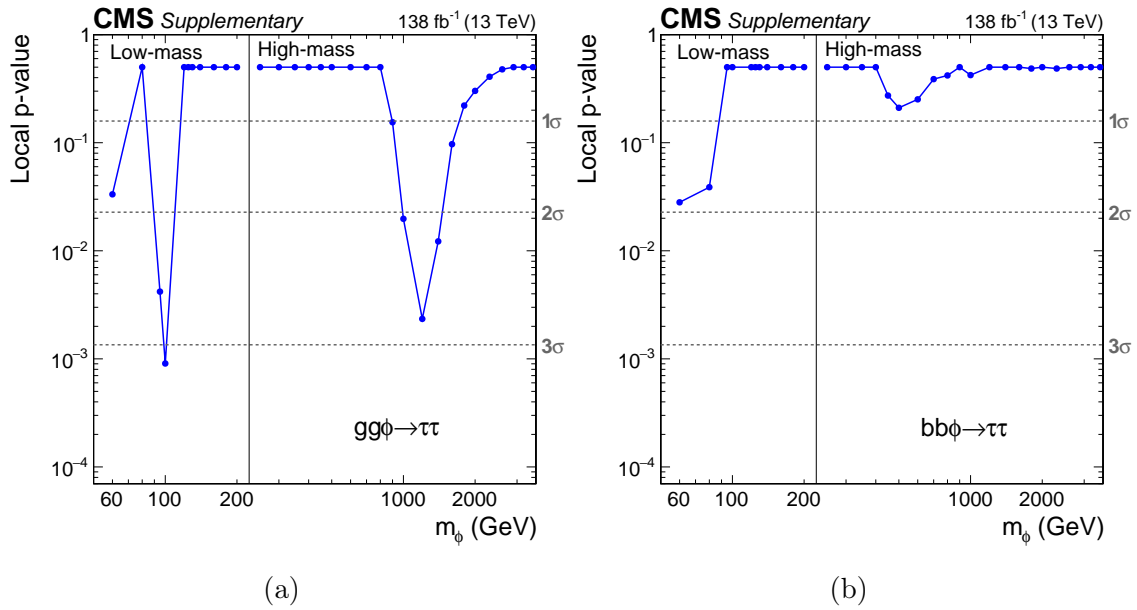


Figure 1.23: Significance.



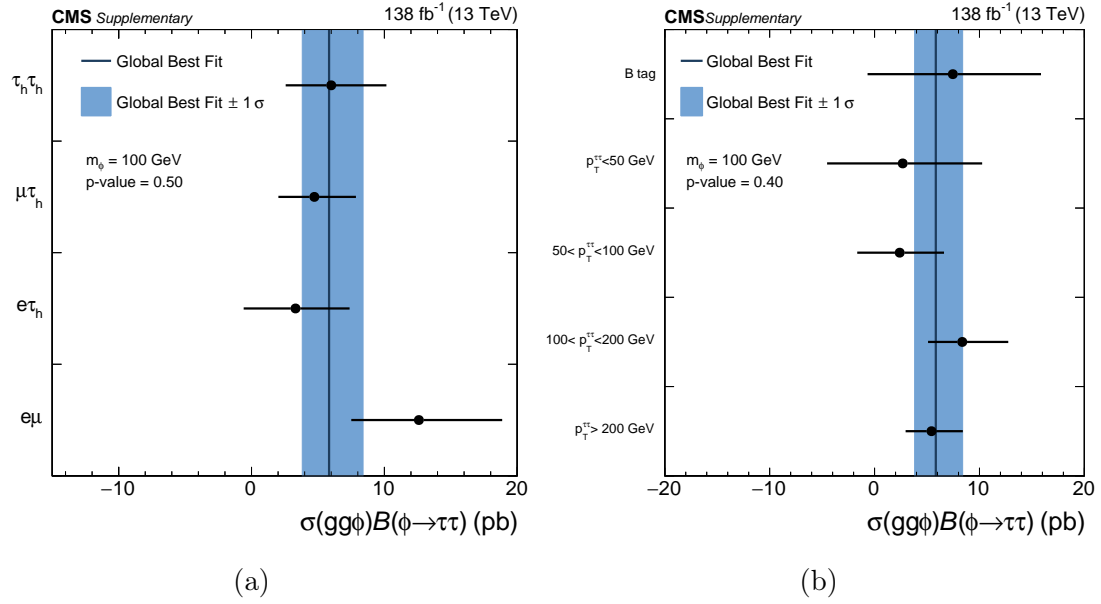


Figure 1.24: Low mass compatibility.

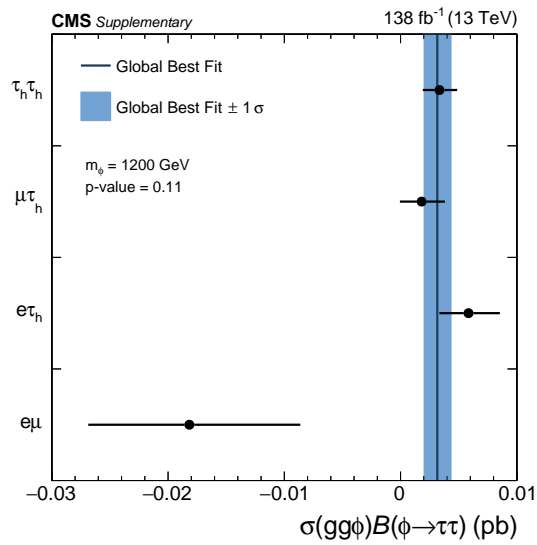


Figure 1.25: High mass compatibility.

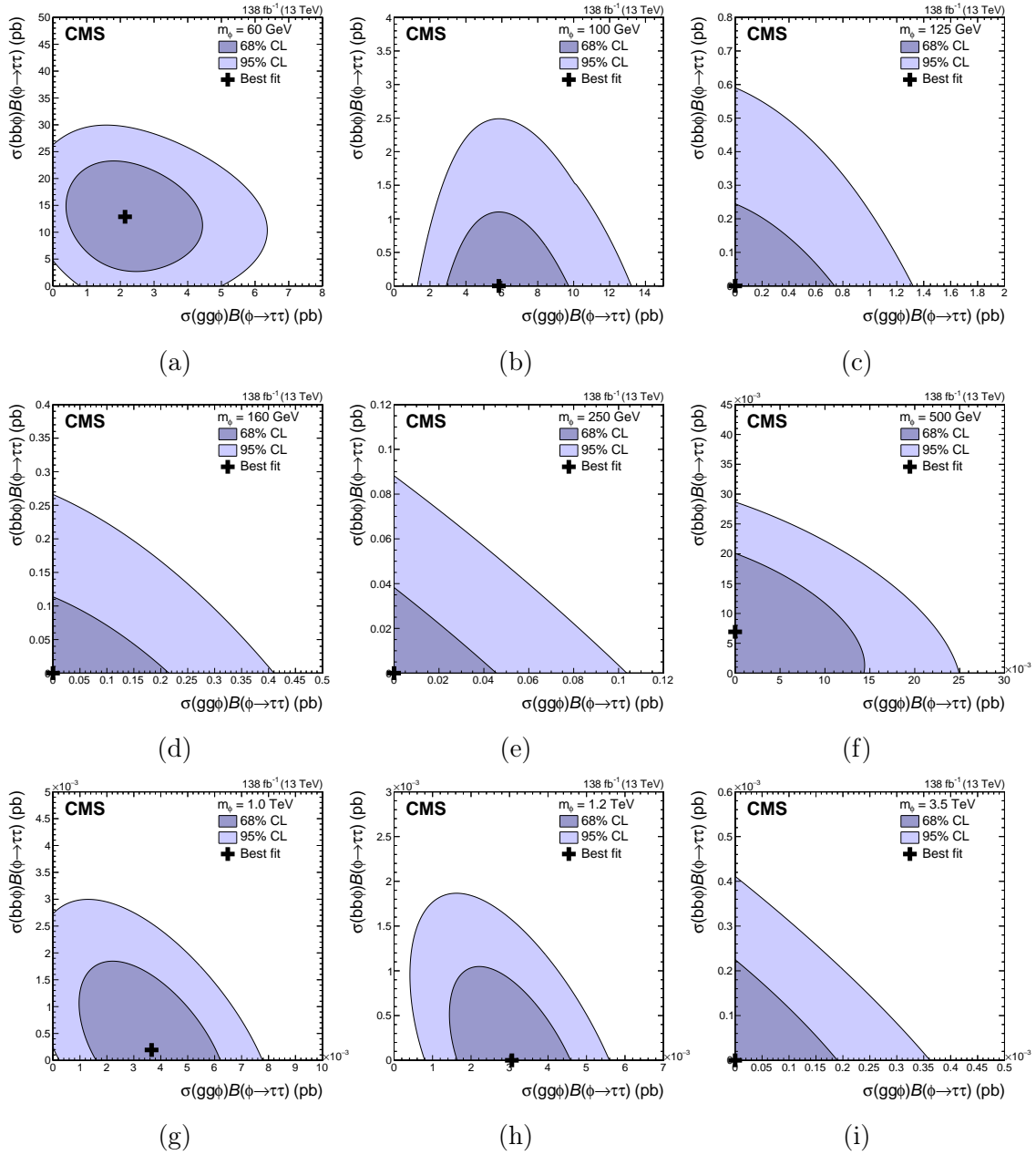


Figure 1.26: 2D Likelihood scans.

## 1.12 Model Dependent Limits

For the hypothesis test the likelihood is

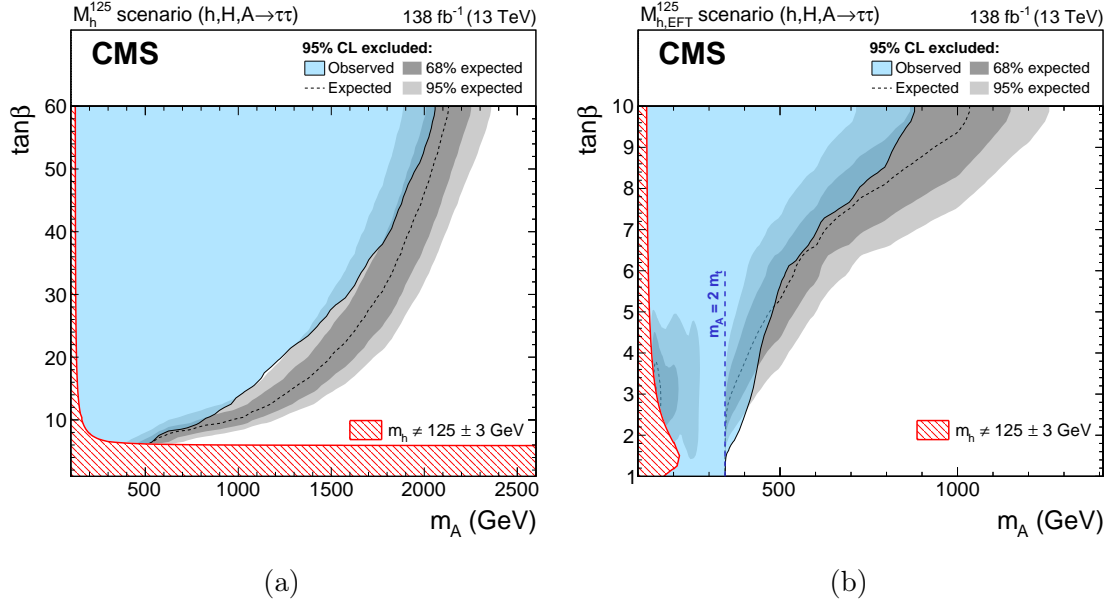


Figure 1.27: MSSM limits.

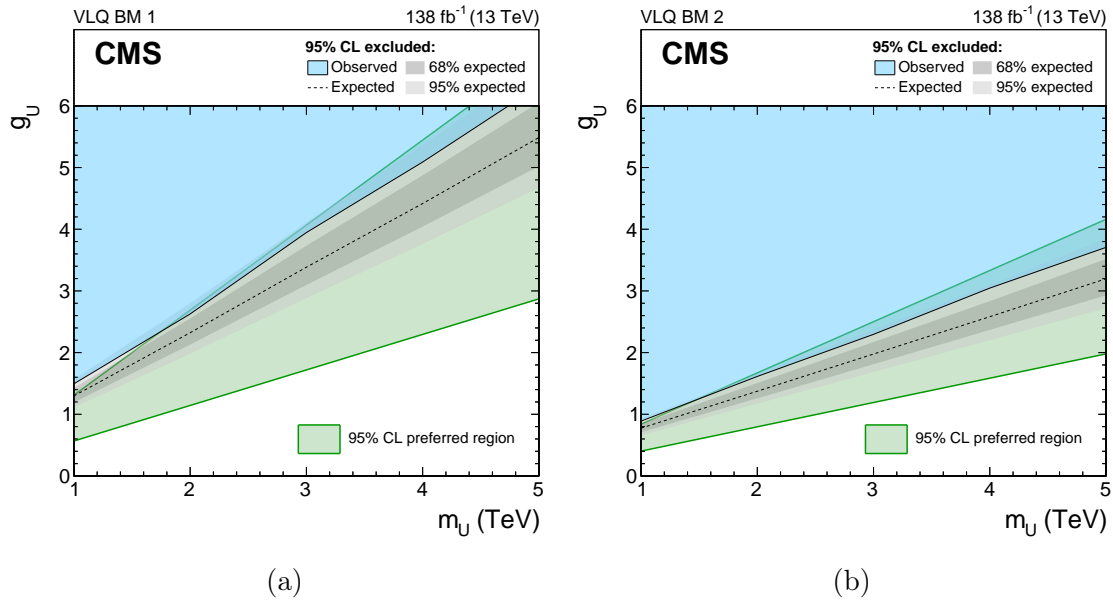


Figure 1.28: VLQ limits.